

# Distributional Uncertainty Analysis and Robust Optimization in Spatially Heterogeneous Multiscale Process Systems

Donovan Chaffart, Shabnam Rasoulia, and Luis A. Ricardez-Sandoval  
Dept. of Chemical Engineering, University of Waterloo, Waterloo, Canada, N2L 3G1

DOI 10.1002/aic.15215

Published online March 15, 2016 in Wiley Online Library (wileyonlinelibrary.com)

*Multiscale models have been developed to simulate the behavior of spatially-heterogeneous porous catalytic flow reactors, i.e., multiscale reactors whose concentrations are spatially-dependent. While such a model provides an adequate representation of the catalytic reactor, model-plant mismatch can significantly affect the reactor's performance in control and optimization applications. In this work, power series expansion (PSE) is applied to efficiently propagate parametric uncertainty throughout the spatial domain of a heterogeneous multiscale catalytic reactor model. The PSE-based uncertainty analysis is used to evaluate and compare the effects of uncertainty in kinetic parameters on the chemical species concentrations throughout the length of the reactor. These analyses reveal that uncertainty in the kinetic parameters and in the catalyst pore radius have a substantial effect on the reactor performance. The application of the uncertainty quantification methodology is illustrated through a robust optimization formulation that aims to maximize productivity in the presence of uncertainty in the parameters. © 2016 American Institute of Chemical Engineers AIChE J, 62: 2374–2390, 2016*

**Keywords:** multiscale modeling, catalytic flow reactors, gap-tooth scheme, uncertainty analysis, power series expansion

## Introduction

The importance of heterogeneous catalytic reactors in chemical processes has inspired a significant amount of research directed toward identifying new catalysts and optimizing existing catalytic processes.<sup>1–3</sup> Model-based catalyst design in particular has emerged as a prominent method to facilitate the manufacturing of optimized catalytic reactors.<sup>4–6</sup> The phenomena that occur in these systems evolve over a wide range of length and time scales, spanning from the macroscopic fluid phase domain to the microscopic catalyst surface domain. Catalytic systems are typically modeled using continuum-based approaches, which can be solved using techniques such as finite difference and finite element analysis.<sup>7–9</sup> Since these models assume surface uniformity, the state of the catalyst surface can be determined through simple mathematical expressions. These models are thus incapable of accounting for surface heterogeneities such as adsorbate lateral interactions and surface defects, and therefore do not provide an adequate description of the microscopic scale. The multiscale integration hybrid algorithm is a practical modeling approach that can capture phenomena occurring over different spatial and temporal scales, which range from the electronic to the macroscopic scale.<sup>10,11</sup> Different domains can be described through a multiscale algorithm that utilizes a lattice-based kinetic Monte Carlo (KMC) model to capture the surface behavior coupled with a continuum model to describe the behavior of the fluid phase. This framework has been used

extensively to model a wide range of multiscale process systems such as thin film growth,<sup>12,13</sup> crystallization,<sup>14,15</sup> copper electrodeposition,<sup>16,17</sup> and spatially homogeneous catalytic reactors.<sup>18–20</sup> This approach accounts for lateral interactions and other surface nonuniformities in catalytic reactors through the lattice-based KMC model. However, this multiscale approach to model the catalytic reactor system still presents challenges that need to be addressed. Lattice-based KMC simulations are stochastic and require large lattice sizes to minimize noise and improve accuracy in the responses. However, employing large lattices is computationally intensive due to the large number of required KMC events, which makes it inefficient for optimization applications. This computational burden can be reduced through the use of parallel computation techniques such as the decomposition-assignment-orchestration parallel computation program.<sup>21</sup> Furthermore, in spatially-heterogeneous multiscale catalytic flow reactors, the transport and reaction of chemical species, together with microscopic events occurring on the catalyst surface inside the reactor, produce concentration gradients that cannot be neglected. These gradients lead to variation in the rates of microscopic surface events, and therefore, the catalytic behavior across the surface domain cannot be modeled using a single KMC model.<sup>11,22</sup> Consequently, multiple KMC lattices must be used to handle variation in the microscopic surface events over the full reactor axial domain.<sup>23</sup> This can be accomplished efficiently by adopting patch dynamics techniques such as the gap-tooth model, where the spatial reactor behavior is evaluated coarsely using a minimal number of KMC lattices.<sup>24,25</sup> Similar techniques, such as the coarse time-stepper methodologies, can also be used to coarsely evaluate the reactor's temporal behavior. This is of particular use when there

Correspondence concerning this article should be addressed to L.A. Ricardez-Sandoval at laricard@uwaterloo.ca

exists no closed-form models to express the macroscopic behavior of the reactor.<sup>26,27</sup>

A key concern in multiscale modeling and optimization of chemical process systems stems from the uncertainty in the model structure and parameters. The reaction pathways that occur in the reactor are often unknown, with potentially undiscovered intermediate steps not taken into consideration. Multiple microkinetic pathways are often proposed that are capable of describing a particular reaction,<sup>28</sup> and therefore the exact pathway is seldom known. Furthermore, due to the limited information available, the values of system parameters are difficult to estimate from experimental results. Alternatively, density functional theory (DFT) can be used to determine the values of the kinetic system parameters<sup>29</sup>; however, these calculations are computationally intensive and subject to truncation errors.<sup>30</sup> Neglecting model-plant mismatch in model-based optimization and control schemes can cause substantial deviations from the predicted reactor performance, which can lead to considerable losses in reactor efficiency.<sup>31–36</sup> It is therefore necessary to develop tools that can efficiently account for uncertainty in multiscale system models. One approach to improve the control performance of the batch processes in the presence of model-plant mismatch is run-to-run control, where data from previous batches is used to update the parameters and reduce the uncertainty.<sup>14,37</sup> Alternatively, uncertainty analysis can be used to directly propagate the parametric uncertainty through the system model without the need of information from prior batch studies. One widely-used framework for uncertainty propagation is the sampling-based Monte Carlo (MC) method. This framework generates a large number of random realizations of the uncertain parameters and uses the primary system model to determine the distribution in the outputs, i.e., the output variability. Due to the large number of required simulations, however, this method can be computationally prohibitive, particularly for online applications in multiscale process systems.<sup>11</sup> As an alternative, mathematical methods such as polynomial chaos expansion (PCE) or power series expansion (PSE) can be employed. PSE and PCE approximate the primary model using low-order mathematical expressions obtained from sensitivity analysis techniques and efficient sampling methods, respectively.<sup>38–40</sup> These tools have been employed in previous studies for robust optimization and predictive control of batch (macroscopic) processes.<sup>41–46</sup>

Notwithstanding the existence of the aforementioned tools, uncertainty analysis in multiscale process systems remains as a challenging and intensive task. Since multiscale models are not available in closed-form, employing methods such as PSE and PCE requires extensive numerical analyses. Due to the stochastic behavior of KMC simulations, it can be challenging to accurately determine the sensitivities necessary for PSE-based uncertainty analysis in these multiscale models. To achieve reasonable accuracy, the sensitivities can be determined by taking the average over multiple model simulations which comes at the cost of increased computational time.<sup>47,48</sup> Therefore, very few studies have addressed the effects of uncertainty in model-based control and robust optimization of multiscale process systems. Rasoulzadeh and Ricardez-Sandoval have proposed an uncertainty analysis framework using PSE, which has been applied for robust optimization and online control of a thin film deposition process using standard proportional integral controllers and advanced model-based control schemes.<sup>35,36,49–51</sup> Nagy and Allgöwer employed a mean-

variance approach to integrate the effects of parametric uncertainty into a robust end-point nonlinear model predictive control scheme for a thin film deposition process.<sup>52</sup> These studies, however, analyze the uncertainty propagation in spatially homogeneous multiscale systems. A small handful of studies have addressed uncertainty in the optimization of heterogeneous multiscale systems, where the effects of uncertainty cannot be assumed to be consistent in the spatial domain. Ulissi et al. used MC sampling methods to propagate parameter uncertainty into a multiscale catalytic plug flow reactor model derived from mean field theory; that analysis was used to determine the optimal catalyst-adsorbate bond energies to maximize the yield of an ammonia decomposition reaction.<sup>53</sup> The computational costs in that approach may be significant due to the MC sampling method used for uncertainty propagation through the reactor model. Furthermore, that work only focused on studying the effects of uncertainty on the overall ammonia conversion at the end of the reactor. Analyzing uncertainty within the reactor, where the effect of parameter uncertainty on the process outputs can vary as a consequence of spatial gradients, necessitates uncertainty analysis at multiple spatial points. To the authors' knowledge, this spatially-variant uncertainty analysis of heterogeneous multiscale systems is lacking in the literature.

Motivated by this realization, the objective of this research is to study the effects of model parameter uncertainties throughout the spatial domain of a heterogeneous multiscale process system. A KMC-continuum multiscale approach is utilized to simulate a porous catalytic flow reactor. Probabilistic uncertainties in the key multiscale model parameters are propagated into the model outputs using PSE, and their effects are analyzed through the variation in the steady state concentrations of all chemically-relevant species. Uncertainty is considered in the kinetic parameters of the surface domain and in the reactor design parameters, i.e., the pore size. This article is structured as follows: The next section provides a description of the multiscale framework used to model a porous catalytic reactor. The following section describes the PSE-based method used to propagate uncertainties through multiscale models. This framework is subsequently used to analyze the effects of parameter uncertainty across the spatial domain of the heterogeneous multiscale catalytic reactor under different scenarios. The proposed uncertainty quantification method presented in this work has been embedded within optimization formulations that aim to specify the optimal operating conditions and design parameters that can improve productivity in the presence of uncertainty in the multiscale model parameters. Concluding remarks are provided at the end.

## Model Development

The porous catalytic reactor studied in this work was adopted from the previous work by Majumder and Broadbelt<sup>24</sup> and it is illustrated in Figure 1. The system consists of a porous inert support to which a catalytic film is affixed. In the multiscale model proposed for this reactor, the pores of the catalytic support are assumed to be perfect cylinders for simplicity. This multiscale model addresses two separate domains of the catalytic reactor: the fluid phase domain and the catalytic surface domain. In the fluid phase domain, the chemical species enter the pores and transport in the radial and axial directions. In the surface domain, chemical species can adsorb onto the catalyst surface, react to form a product, or desorb back into the fluid phase. The mass transport in the fluid phase

is described through continuum modeling, while the catalyst surface is captured using lattice-based KMC simulations.

### Fluid phase transport model

The transport phenomena in the fluid phase have been described through continuum modeling. The fluid phase transport in a perfectly cylindrical pore is modeled using a two-dimensional rectangular Cartesian geometry for simplicity. The system is assumed to be at thermal equilibrium, and the fluid velocity is assumed to remain constant throughout the reactor. Thus, the fluid phase mass transport equation can be described as follows:

$$u \frac{\partial C_{i,fluid}}{\partial z} = D_i \frac{\partial^2 C_{i,fluid}}{\partial y^2} \quad (1)$$

The boundary conditions are as follows:

$$C_{i,fluid} = C_{i,0}, \quad y > 0, \quad z = 0 \quad (2)$$

$$\frac{\partial C_{i,fluid}}{\partial y} = 0, \quad y = 0, \quad z \geq 0 \quad (3)$$

$$D_i \frac{\partial C_{i,fluid}}{\partial y} = -K_{a,i} C_{i,fluid} \left( 1 - \sum_{j=1}^n \theta_j \right) + K_{d,i} \theta_i e^{-\left( \frac{E_{d,i}}{R_g T} \right)}, \quad (4)$$

$$y = R, \quad z \geq 0$$

In the equations above,  $u$  denotes the fluid's local velocity;  $C_{i,fluid}$  is the fluid phase concentration of the  $i^{\text{th}}$  species;  $D_i$  is the diffusivity of the  $i^{\text{th}}$  species;  $K_{a,i}$  and  $K_{d,i}$  denote the adsorption and desorption constants for the  $i^{\text{th}}$  species, respectively; and  $E_{d,i}$  denotes the activation energy of desorption for species  $i$ . Furthermore,  $T$  denotes the temperature of the system,  $R_g$  denotes the universal gas constant,  $\theta_i$  denotes the surface coverage of species  $i$ , and  $n$  denotes the total number of surface species.  $C_{i,0}$  is defined as the input concentration for species  $i$  at the pore entrance ( $z=0$ ). Similarly, the output concentration for species  $i$ , i.e.,  $C_{out,i}(0,L)$ , is defined as the concentration at the end of the pore toward the center ( $y=0, z=L$ ). Equation 4 is not valid for chemical species that participate directly in surface reactions from the fluid phase. The net flux for these species must be determined directly from their rates of formation and consumption, i.e.,

$$D_f \frac{\partial C_{f,fluid}}{\partial y} = w_{prod,f} - w_{cons,f}, \quad y = R, \quad z \geq 0 \quad (5)$$

In this equation,  $D_f$  and  $C_{f,fluid}$  represent the diffusivity and concentration of any species  $f$  in the fluid phase, whereas  $w_{cons,f}$  and  $w_{prod,f}$  represent the rates of consumption and production of fluid species  $f$  on a single catalyst site, respectively. The consumption/production rates in Eq. 5 and the surface coverage terms in Eq. 4 must be determined from the catalyst surface behavior. As a result, the partial differential equation presented in Eq. 1 cannot be solved without knowledge from the catalyst surface kinetic models.

### Catalyst surface kinetic models

Events taking place at the catalyst surface must be modeled using molecular simulations such as mean-field and KMC as they cannot be adequately captured using continuum models. In the mean-field approximation, adsorbed molecules are assumed to be homogeneously distributed on the surface, and the surface coverages can be determined directly by solving a series of algebraic equations. This approach provides a rela-

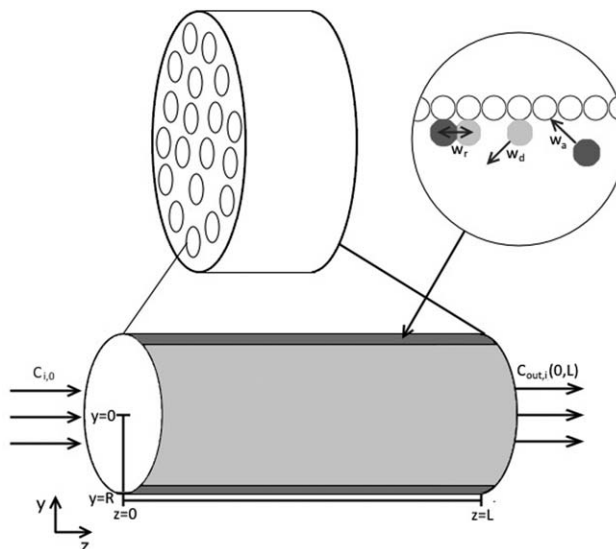
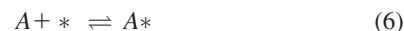


**Figure 1. Schematic of a catalytic reactor with cylindrical pores.**

tively simple model to approximate the events occurring on the catalyst surface. However, this model assumes infinite diffusion across the surface; consequently, it does not explicitly take into account the lateral interactions that are relevant for most catalytic reactions.<sup>24,54,55</sup> KMC is a numerical approach that provides an approximation to the chemical master equation and is able to individually model the surface events taking place on the catalytic surface. Lattice-based KMC simulations utilize a surface lattice to model the molecule configurations on the catalyst surface, which can be used to directly account for lateral adsorbate interactions.<sup>55–57</sup>

The KMC method employed in this work represents the catalyst surface as a finite-sized square lattice with periodic boundary conditions. Each catalyst surface site is assumed to adsorb only a single molecule, and for simplicity, catalytic surface reactions are limited to first nearest neighbour interactions. The catalytic behavior implemented in this work considers a bimolecular kinetic reaction between two different adsorbed reactant molecules resulting in a single product molecule in the fluid phase. The bimolecular reaction mechanism is as follows:



In Eqs. 6–8, A and B represent the reactant species in the fluid phase whereas C represents the product species. Additionally, \* and \*\* represent single and double empty sites on the catalyst, respectively; A\* and B\* represent the adsorbed forms of A and B. For this reaction mechanism, three microscopic surface events have been considered: adsorption of the reactants from the fluid phase onto the catalyst surface, desorption of the chemical species into the fluid phase, and the irreversible reaction between reactants A and B to form product C. According to the kinetic theory of ideal gases,<sup>58</sup> the rate of adsorption takes the following form:

$$W_{a,i}(z) = N_e k_{a,i} C_i(R, z) \quad (9)$$

Here,  $W_{a,i}(z)$  represents the total rate of adsorption for the  $i^{\text{th}}$  species located at axial distance  $z$  from the pore entrance.



$N_e$  denotes the number of empty sites on the lattice, while  $k_{a,i}$  denotes the adsorption rate constant.  $C_i(R, z)$  is the concentration of species  $i$  at an axial distance  $z$  and a radial distance  $R$ , which corresponds to the radius of the pore, i.e.,  $y=R$ . The concentration  $C_i(R, z)$  must be determined from the mass transport model shown in Eq. 1. Consequently, the fluid phase behavior affects the adsorption rate on the catalyst surface. Coupling techniques are required to link these sub-domains together as will be described in the next subsection.

The rate of desorption is considered to follow the Arrhenius type equation, and is calculated as follows:

$$W_{d,i}(z) = N_i k_{d,i} e^{-\frac{E_{d,i}}{R_g T}} \quad (10)$$

In this equation,  $W_{d,i}(z)$  is the total rate of desorption for species  $i$  at distance  $z$  from the pore entrance;  $N_i$  is the total number of sites occupied by species  $i$  on the simulated surface,  $k_{d,i}$  represents the desorption constant for species  $i$ , and  $E_{d,i}$  is the activation energy associated with desorption of species  $i$ . Note that  $k_{d,i}$  and  $k_{a,i}$  from Eq. 9 are related to the rate constants  $K_{d,i}$  and  $K_{a,i}$  from Eq. 4, and can be converted according to the following formulation:

$$K_{x,i} = \frac{C_s}{N_A} k_{x,i} \quad (11)$$

where  $x = \{d, a\}$ ,  $C_s$  is the site concentration on the catalyst surface, and  $N_A$  is Avogadro's number.

The reaction rate depends on the number of surface reactant ensembles on the lattice. A surface reactant ensemble can be defined as a group of reactants that are within close enough proximity to each other on the catalyst surface to react.<sup>55</sup> For the bimolecular mechanism considered in this work, the surface reactant ensemble consists of two molecules of species A and B adjacently adsorbed on the catalyst surface, as shown in Figure 2. Taking this into consideration, the rate of reaction takes the following form:

$$W_r(z) = N_{AB} k_r e^{-\frac{E_r}{R_g T}} \quad (12)$$

Here,  $W_r(z)$  is the total rate of reaction at a distance  $z$  from the entrance of the pore,  $N_{AB}$  is the total number of surface reactant ensembles,  $k_r$  denotes the reaction constant, and  $E_r$  is the activation energy for the reaction. Since the surface reactant ensembles are allowed to form in any four directions on the lattice surface as depicted in Figure 2,  $N_{AB}$  in Eq. 12 accounts for all these ensembles.

Once the kinetic rates have been determined, MC sampling can be utilized to select the event that will occur. To that end, two random values are generated from a standard uniform distribution to select an event and where the event will occur on the surface lattice. The selected event is executed and the time is incremented as follows:

$$dt = \frac{-\ln(\zeta)}{\sum_i [W_{a,i}(z) + W_{d,i}(z)] + W_r(z)} \quad (13)$$

Here,  $dt$  is the time increment approximated for the KMC event, while  $\zeta$  is a randomly-generated number selected from a standard uniform distribution.

### Model coupling

The fluid phase continuum model and the catalytic surface KMC model are coupled through the rate of adsorption given by Eq. 9 and the surface boundary condition depicted in Eq. 4.

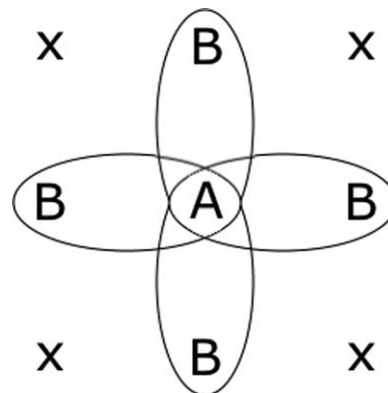


**Figure 2. Four A-B surface reactant ensembles on a KMC lattice.**

The concentration of the chemical species in the fluid phase have a significant impact on the rate of adsorption of the catalyst surface domain, and therefore the concentration term  $C_i(R, z)$  in Eq. 9 is obtained from the solution of the continuum expression in Eq. 1. Conversely, the microscopic phenomena occurring on the catalyst affect the concentration of species in the fluid phase through the coverage of adsorbates on the catalyst surface. These coverages are key to determine the flux of each species along the surface, which is necessary to solve for the fluid phase mass transport equation shown in Eqs. 1–5. The coverage of species  $i$  is determined as follows:

$$\theta_i = \frac{N_i}{N_t} \quad (14)$$

where  $N_i$  represents the total number of sites occupied by species  $i$  on the surface and  $N_t$  represents the total number of lattice sites. The coverage-based approach cannot be used to calculate the flux for species C, which exists only in the fluid phase. Alternatively, the flux can be determined by the rates of consumption and production,  $w_{cons,f}$  and  $w_{prod,f}$ , as demonstrated in Eq. 5. These rates can be estimated as follows:

$$w_{e,f} = \frac{M_{e,f}}{N_t \sum_{j=1}^N dt_j}, \quad (15)$$

where  $e = \{cons, prod\}$ ;  $M_{e,f}$  denotes the number of molecules of species  $f$  in the fluid phase that are consumed or produced on  $N_t$  surface sites during a pre-determined number of surface events  $N$ ; and  $dt_j$  denotes the time increment for surface event  $j$  as calculated in Eq. 13. In the bimolecular reaction considered in this work, species C is not consumed, and therefore the consumption term  $w_{cons,f}$  is neglected. The values of all the model parameters used in this work are derived from the previous work of Dooling and Broadbelt<sup>55</sup> as listed in Table 1.

### Gap-tooth approximation

Porous catalytic reactors are spatially heterogeneous systems, where the transport of chemical species creates concentration gradients along the reactor's axial length. As a result, spatially heterogeneous multiscale techniques are required to take these gradients into account. The gap-tooth method proposed by Kevrekidis et al.<sup>59–63</sup> is a technique that has been used to describe spatial heterogeneities in catalytic reactor systems. In this framework, the entire spatial domain is subdivided into periodically-spaced patches, referred to as teeth, separated by spaces referred to as gaps. Each tooth is simulated with an independent KMC lattice that is employed to

**Table 1. Multiscale Model Parameters**

Parameter	Symbol	Value
Pore length	$L$	100 nm
Pore radius	$R$	10 nm
Fluid velocity	$u$	0.01 m/s
Fluid diffusivity	$D_i$	$5.3 \times 10^{-9}$ m <sup>2</sup> /s
Initial concentration, species A	$C_{A,0}$	241 mM
Initial concentration, species B	$C_{B,0}$	241 mM
Initial concentration, species C	$C_{C,0}$	0 M
Boundary condition adsorption constant, species A	$K_{a,A}$	$2.0757 \times 10^{-6}$ mol-m/(M·L·s)
Surface model adsorption constant, species A	$k_{a,A}$	1 molecule/(M·site·s)
Boundary condition adsorption constant, species B	$K_{a,B}$	$2.0757 \times 10^{-6}$ mol-m/(M·L·s)
Surface model adsorption constant, species B	$k_{a,B}$	1 molecule/(M·site·s)
Boundary condition desorption constant, species A	$K_{d,A}$	$2.0757 \times 10^4$ mol-m/(L·s)
Surface model desorption constant, species A	$k_{d,A}$	$1 \times 10^{10}$ molecule/(site·s)
Boundary condition desorption constant, species B	$K_{d,B}$	$2.0757 \times 10^4$ mol-m/(L·s)
Surface model desorption constant, species B	$k_{d,B}$	$1 \times 10^{10}$ molecule/(site·s)
Activation energy of desorption, species A	$E_{d,A}$	95 kJ/mol
Activation energy of desorption, species B	$E_{d,B}$	100 kJ/mol
Surface model reaction constant	$k_r$	$2 \times 10^6$ molecule/(site·s)
Activation energy of reaction	$E_r$	57 kJ/mol
Temperature	$T$	500 K
Number of catalyst sites per lattice	$N_T$	900 sites
Site concentration	$C_s$	$1.25 \times 10^{18}$ (sites-m)/L

determine the specific surface coverages at its location within the reactor. The teeth are considered to be infinitesimal, such that the effects of the concentration gradient on a single tooth can be assumed to be negligible. Conversely, the gaps are treated coarsely and the coverages across each gap are approximated using cubic interpolation. Figure 3 shows the gap-tooth model implemented in this work. The catalyst surface considered in this study is subdivided into eight teeth separated by 125 nm gaps. The number of teeth was determined such that they provide sufficient accuracy in the results without substantial computational cost. The first tooth is considered at the reactor entrance ( $z=0$ ), and the eighth tooth is considered at the reactor's outlet ( $z=L$ ). The process begins by “lifting” concentrations out of the fluid phase at each tooth location on the catalyst surface to calculate the adsorption rates. The catalyst surface at each tooth is allowed to evolve using independent KMC simulations, i.e., each tooth has its own lattice-based KMC model representing the catalyst surface at that particular point in the reactor's spatial domain. The coverages and fluxes are extracted at each tooth and used by interpolation techniques to approximate the coverages and fluxes across each gap. The process concludes through “restriction,” where the complete set of coverages and fluxes are returned to the fluid phase model through the boundary conditions presented in Eqs. 4 and 5.

#### Lattice size determination and solution approach

Due to the stochastic nature of the KMC simulations, the responses obtained from the multiscale model can be noisy depending on the lattice size. Larger lattices produce more accurate results, as stochastic fluctuations have less impact due to the increased number of sites. However, larger lattices require more KMC event steps to reach the same integration times as smaller lattices, which results in additional computational costs. Therefore, a lattice size that provides enough accuracy while still maintaining a low computational cost must be specified through offline analysis. Figure 4 shows the evolution of the surface coverage for species A on the first tooth approximated using  $30 \times 30$ ,  $100 \times 100$ , and  $200 \times 200$  KMC lattice sizes. The  $30 \times 30$  lattice is able to capture the general behavior of the surface evolution process; however,

the noise in the response impedes accurate determination of the surface coverage values. Alternatively, larger lattices provide a good approximation of the surface evolution during the KMC simulation with minimal noise. No significant improvement is observed between the  $100 \times 100$  and  $200 \times 200$  lattice sizes. However, both larger lattices require significantly more computational time compared to the  $30 \times 30$  lattice as can be seen in the computational times recorded in the caption of Figure 4. To improve the accuracy of the smaller lattice-size KMC simulations without gaining significant additional computational time, the results from eight independent  $30 \times 30$  lattice KMC simulations are averaged and compared to the previous simulation results. This averaging technique has been used in previous works to reduce the noise produced by smaller KMC lattices.<sup>35,64</sup> As shown in Figure 4, the noise in the coverage of species A using the averaged  $30 \times 30$  lattices is comparable to the noise of the result obtained from a  $100 \times$

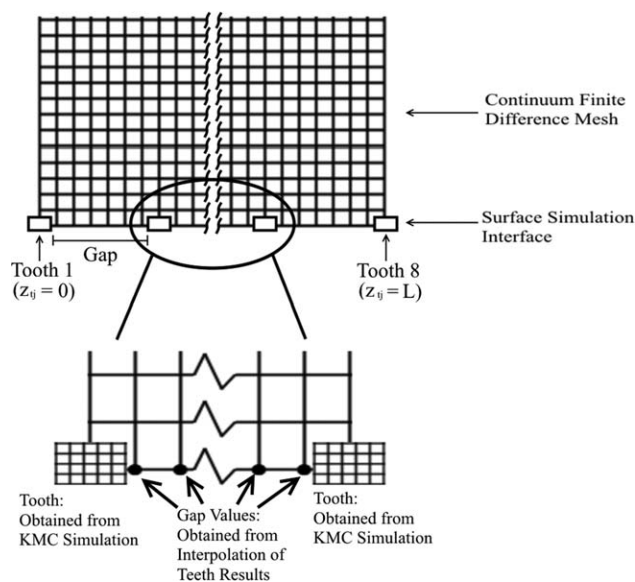


**Figure 3. The gap-tooth scheme for the catalytic surface of the reactor.**

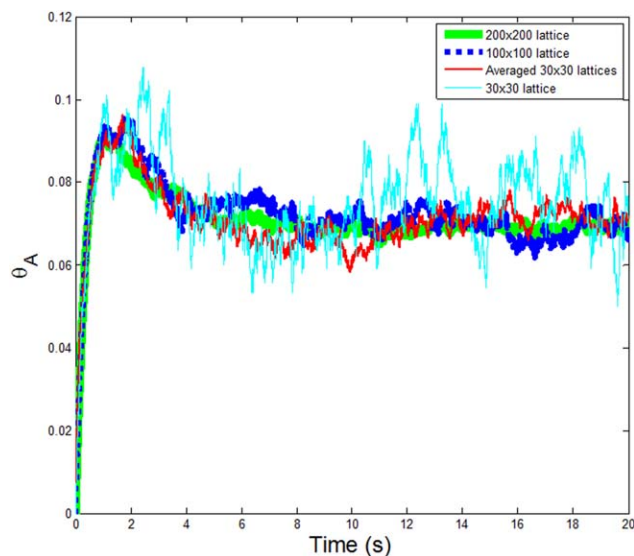


**Figure 4. Comparison of the surface coverage evolution of species A at the first reactor tooth using  $30 \times 30$  (1 s),  $100 \times 100$  (21 s),  $200 \times 200$  (422 s), and an average of eight  $30 \times 30$  (3 s) lattices in the KMC simulations.**

[Color figure can be viewed in the online issue, which is available at [wileyonlinelibrary.com](http://wileyonlinelibrary.com).]

100 lattice. Furthermore, as presented in the caption of Figure 4, the computational time for the averaged  $30 \times 30$  lattice approach is significantly lower as compared to the higher lattice sizes. The present work, therefore, employs the average of eight independent multiscale simulations utilizing  $30 \times 30$  KMC lattice sizes to represent the evolution of the surface catalyst. The computational time can also be reduced without significant loss of accuracy in the KMC simulation results by decoupling the predominant kinetic events and treating them deterministically.<sup>65,66</sup> This approach is most practical for fast kinetic events, e.g., surface diffusion, which may account for the majority of the KMC computational time. However, this approach is not applicable for the present multiscale reactor model, since the adsorption of species A and B are the surface events that consume most of the computational cost in the KMC simulation, i.e., roughly 28% for each species adsorp-

tion. These events cannot be decoupled from the rest of the kinetic surface events since the rate of reaction depends on the location of molecules on the surface, which are directly affected by the adsorption events of species A and B.

In this work, a time-independent multiscale model is used to simulate the steady state fluid concentrations of the reactor. Before the fluid phase model is updated, KMC is evolved on each of the eight lattices (i.e., one for each tooth) until steady state is reached. It is assumed that the steady state is attained when the change in the surface coverages at each tooth falls below a certain threshold (e.g., below 5%) over at least 1000 KMC events. When steady state is reached in the KMC simulations, the surface coverages are used to solve for the fluid phase mass transport equation presented in Eqs. 1–5. The KMC noise in the results is reduced by using an average of coverages over the last 1000 KMC events. The mass transport model is solved using a finite difference approach with 101 discretization points in the axial direction and 43 points in the radial direction. Increasing the spatial discretization in the fluid phase mass transport model does not improve the accuracy in the calculations. The concentrations obtained from the finite difference code are employed in the adsorption rates to update the KMC model. This is repeated until the maximum variation in the species concentrations at each point ( $y, z$ ) within the reactor model is less than 5%. The present multiscale model was validated through comparison to previous results reported by Majumder and Broadbelt, using the parameter values reported in their work.<sup>24</sup>

Simulating the model using the nominal parameter values listed in Table 1 required on average 8000 KMC events and approximately 1 s of CPU time for each tooth lattice to reach a local steady state (3.4 GHz Intel i7-3770 processor). Furthermore, it takes about 6 s on average to perform a multiscale model cycle consisting of one complete simulation for both the catalyst surface domain and the fluid phase domain. A single run of the multiscale model requires on average 7 cycles and about 40 s of CPU time to compute.

The concentration profiles obtained through simulation of the multiscale catalytic reactor model using the parameter values listed in Table 1 are shown with the green lines in Figure 5. In porous catalytic flow reactors, however, the size of the pores plays a significant role in the reactor performance. To briefly investigate this behavior, axial concentration profiles

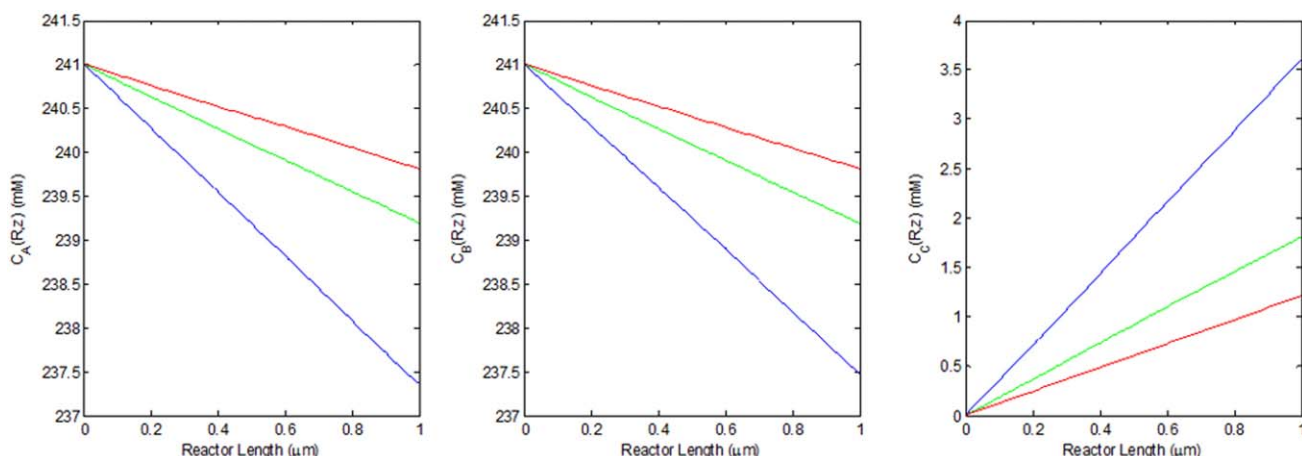


**Figure 5. Axial concentration profiles on the catalyst surface ( $y=R$ ) for each species using nominal model parameters with pore sizes of 5 nm (blue), 10 nm (green), and 15 nm (red).**

[Color figure can be viewed in the online issue, which is available at [wileyonlinelibrary.com](http://wileyonlinelibrary.com).]



obtained from reactors with pore radii of 5 nm and 15 nm are also shown in Figure 5. As illustrated in this figure, the axial concentration profiles for product C obtained from the reactors with smaller pores are significantly larger. Reducing the pore sizes increases the surface-to-volume ratio within the catalytic reactor which results in an improvement in catalyst performance. Since the catalyst surface behavior is independent of the size of the pore, any surface events that take place will have a larger impact on the concentrations within smaller pores, resulting in higher concentrations of product C for the considered bimolecular reaction. Further analysis of Figure 5 reveals that linear changes in the pore radius size results in nonlinear changes in the concentrations of the chemical species, as a result of the quadratic relationship between the pore radius and its volume.

## Uncertainty Analysis Using PSE

Distributional uncertainty propagation can be performed on the porous catalytic reactor model detailed previously by replacing the primary multiscale model with a low-order approximation such as PSE or PCE. Employing these approaches, the variability in the model outputs with respect to the uncertain parameters is approximated by constructing a low-order model of the system. These approximations are computationally efficient thus facilitating uncertainty propagation in the process outputs, which is accomplished using MC sampling techniques applied to the low-order models. PCE is an effective uncertainty quantification method for highly nonlinear processes that consider multiple uncertain parameters, since analytical expressions can be determined using Galerkin's projection. However, models that are not available in closed-form such as the present heterogeneous multiscale model reactor require the implementation of non-intrusive methods. Depending on the model's degree of nonlinearity and the number of uncertain parameters considered, non-intrusive PCE may require the implementation of advanced sampling techniques and simulation of a large number of samples, which will impact the computational costs associated with this method. Conversely, PSE only relies on the sensitivities of the outputs with respect to the uncertain parameters to construct a low-order model of the system, which is practical for this application. The use of sensitivities is a common practice as it requires minimal sampling from the multiscale model and therefore the computational cost for PSE remains reasonable regardless of the model complexity. Needless to say, the computational cost for PSE depends on the number of uncertain parameters and the number of terms considered in the PSE, which both require the calculation of additional sensitivities to construct representative low-order models.<sup>67,68</sup> Adding more terms to the PSE can improve the accuracy of the PSE-based approximation<sup>35,36,38</sup> and the number of terms required for reasonable accuracy depends on the degree of nonlinearity of the system model. Higher-order series expansions improve the model predictions but result in higher computational costs due to the computation of additional higher-order sensitivity terms. The order of the PSE required to approximate the model must therefore be determined offline through direct comparison to the primary model. In spatially heterogeneous multiscale systems, a single uncertainty analysis is not sufficient to explicitly describe the effects of uncertainty throughout the spatial domain of the model. PSEs must subsequently be constructed at multiple discrete spatial points within the reactor to establish a comprehensive understanding of the effects of

uncertainty. Accordingly, a step-by-step PSE-based uncertainty propagation algorithm for spatially heterogeneous multiscale systems has been used in this study and is as follows:

1. Discretize the radial direction of catalytic reactor ( $0 < y < R$ ), into finite number of discrete radial points,  $y_{ii}$ , and the axial direction ( $0 < z < L$ ) into finite number of axial points,  $z_{ij}$ .
2. Define  $\boldsymbol{\varphi} = [\varphi_1, \dots, \varphi_m, \dots, \varphi_M] \in \mathbb{R}^M$  as the vector of uncertain parameters,  $\hat{\boldsymbol{\varphi}} = [\hat{\varphi}_1, \dots, \hat{\varphi}_m, \dots, \hat{\varphi}_M] \in \mathbb{R}^M$  as the vector of nominal parameters,  $\boldsymbol{\omega}(y_{ii}, z_{ij}) = [\omega_1(y_{ii}, z_{ij}), \dots, \omega_n(y_{ii}, z_{ij}), \dots, \omega_N(y_{ii}, z_{ij})] \in \mathbb{R}^N$  as the vector of system outputs at spatial point  $(y_{ii}, z_{ij})$ , and  $\hat{\boldsymbol{\omega}}(y_{ii}, z_{ij}) = [\hat{\omega}_1(y_{ii}, z_{ij}), \dots, \hat{\omega}_n(y_{ii}, z_{ij}), \dots, \hat{\omega}_N(y_{ii}, z_{ij})] \in \mathbb{R}^N$  as the vector of nominal outputs at point  $(y_{ii}, z_{ij})$ .
3. Specify the multivariate probability distribution function (PDF) for the vector of uncertain parameters  $\boldsymbol{\varphi}$ ,  $f_{pd}(\boldsymbol{\varphi})$ , such that,

$$\boldsymbol{\varphi} = \{\boldsymbol{\varphi} | \boldsymbol{\varphi} \in f_{pd}(\boldsymbol{\varphi})\} \quad (16)$$

This indicates that any realization for the vector of uncertain parameters follows a pre-defined PDF with specific known statistical characteristics, such as mean and variance.

4. Determine the sensitivities of each system output at every spatial point with respect to the uncertain parameters. The first and second-order sensitivities can be obtained as follows:

$$\mathbf{J}_n(y_{ii}, z_{ij}) = \left( \frac{\partial \omega_n(y_{ii}, z_{ij})}{\partial \boldsymbol{\varphi}} \right)_{\boldsymbol{\varphi}=\hat{\boldsymbol{\varphi}}}, \quad \mathbf{M}_n(y_{ii}, z_{ij}) = \left( \frac{\partial^2 \omega_n(y_{ii}, z_{ij})}{\partial \boldsymbol{\varphi}^2} \right)_{\boldsymbol{\varphi}=\hat{\boldsymbol{\varphi}}} \quad (17)$$

5. Build a PSE model for each system output,  $\omega_n(y_{ii}, z_{ij})$ , using the sensitivities calculated from the previous step, i.e.,

$$\begin{aligned} \omega_n(y_{ii}, z_{ij}) &= \hat{\omega}_n(y_{ii}, z_{ij}) + \mathbf{J}_n(y_{ii}, z_{ij})(\boldsymbol{\varphi} - \hat{\boldsymbol{\varphi}}) \\ &+ \frac{1}{2}(\boldsymbol{\varphi} - \hat{\boldsymbol{\varphi}})^T \mathbf{M}_n(y_{ii}, z_{ij})(\boldsymbol{\varphi} - \hat{\boldsymbol{\varphi}}) + \dots \end{aligned} \quad (18)$$

Note that higher order terms can be added to the PSE model provided that their corresponding sensitivities have been computed in Step 4.

6. Propagate the uncertainties into the system output at each discrete spatial point,  $\omega_n(y_{ii}, z_{ij})$  using the expansion shown in Eq. 18 by generating MC samples from the PDF  $f_{pd}(\boldsymbol{\varphi})$  for the vector of uncertain parameters,  $\boldsymbol{\varphi}$ . This will result in a PDF,  $f_{pd}(\omega_n(y_{ii}, z_{ij}))$  that represents the effect of uncertain parameters on the system output at the point  $(y_{ii}, z_{ij})$ .
7. Compute upper and lower bounds on  $\omega_n(y_{ii}, z_{ij})$ , i.e.,  $\omega_n^{up}(y_{ii}, z_{ij})$  and  $\omega_n^{low}(y_{ii}, z_{ij})$ , respectively, at a given confidence level,  $\alpha$ , according to:

$$\begin{aligned} \omega_n^k(y_{ii}, z_{ij}) &= F^{-1}(P | \omega_n(y_{ii}, z_{ij})) = \{\omega_n(y_{ii}, z_{ij}) : F(\omega_n(y_{ii}, z_{ij}))\}, \\ P &\in \left\{1 - \frac{\alpha}{2}, \frac{\alpha}{2}\right\} \text{ for } k \in \{up, low\} \end{aligned} \quad (19)$$

where  $F^{-1}(P | \omega_n(y_{ii}, z_{ij}))$  is the empirical inverse cumulative distribution function evaluated at a probability limit,  $P$ . If  $P$  is set to  $1 - \frac{\alpha}{2}$  and  $\frac{\alpha}{2}$ , one can obtain the upper and lower bounds on the output,  $\omega_n^{up}(y_{ii}, z_{ij})$  and  $\omega_n^{low}(y_{ii}, z_{ij})$ , respectively. The empirical cumulative distribution function for each output is obtained from the corresponding cumulative frequency histogram. To calculate the histogram of the output, the range of the output

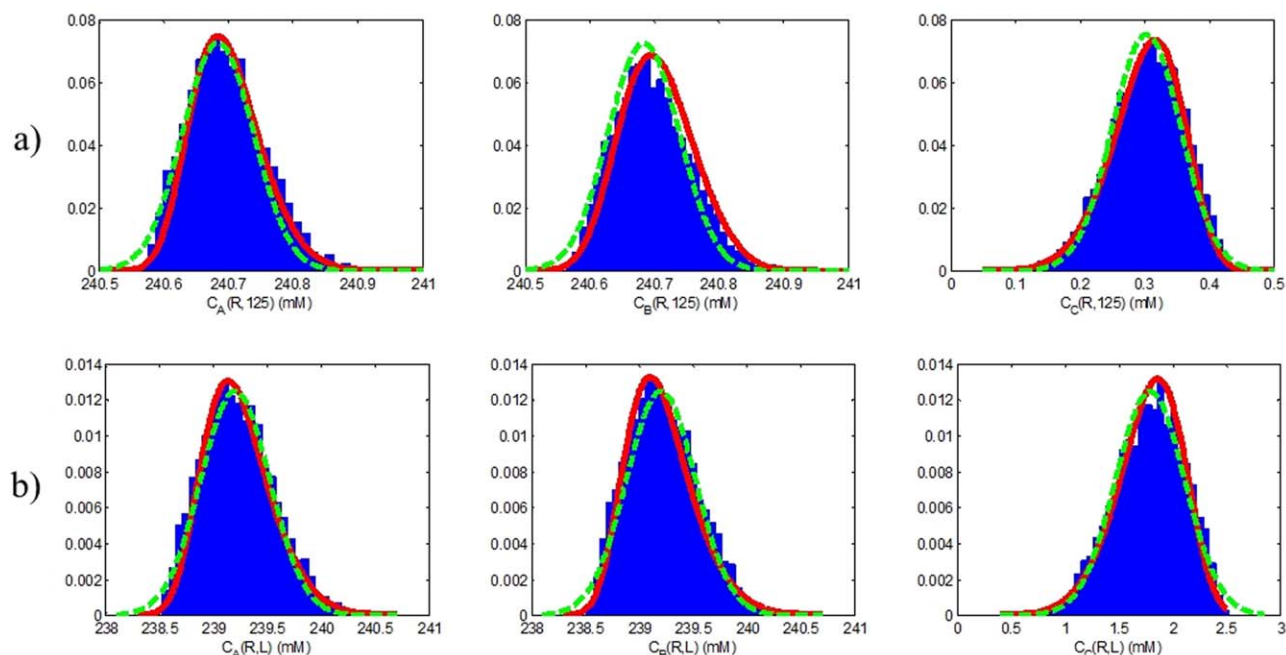


**Figure 6. PDFs of the fluid concentrations near the catalyst surface (a) at the second tooth ( $y=R$ ,  $z = 125$  nm), and (b) at the last tooth ( $y=R$ ,  $z=L$ ). The PDFs were generated using 1000 MC sampling points applied to the primary multiscale model (in blue), the first-order PSE (in green), and the second-order PSE (in red).**

[Color figure can be viewed in the online issue, which is available at [wileyonlinelibrary.com](http://wileyonlinelibrary.com).]

data is divided into bins of equal widths and the number of data points that fall into each bin is counted. The cumulative probability at point  $\omega_n(y_{ii}, z_{ij})$  is then approximated by dividing the cumulative summation of the sample points falling into the first bin up to the bin that encompasses  $\omega_n(y_{ii}, z_{ij})$  by the total number of sample points.

The multiscale model used in this work is stochastic; therefore, stochastic sensitivity is required to compute the gradients in the PSE approximations. As discussed in the previous section, the stochastic noise was reduced by taking the average over multiple model simulations with the same parameter values and using the averaged responses to calculate the sensitivities. A larger number of sample points for each average leads to more accurate results at the cost of additional computational time. This trade-off was addressed within this work by taking the average over eight simulations of the multiscale model performed in parallel, which was determined to provide reasonably accurate results at acceptable computational costs.

To investigate the performance of the proposed framework for the multiscale catalytic reactor, an uncertainty analysis has

been performed with respect to the desorption activation energy for species A,  $E_{d,A}$ , which affects the rate of desorption represented by Eq. 10. The uncertainty in  $E_{d,A}$  was assumed to take the form of a normal distribution around the nominal value (95 kJ/mol) with a standard deviation of 3% of the nominal value. The uncertainty analysis was performed to compare first-order and second-order PSE-based approaches to the MC applied to the primary multiscale reactor model. For this comparison, 1000 MC sample points of the desorption activation energy were used to propagate uncertainty into the output concentrations of each species using the primary model. As shown in Figure 6, the uncertainty was propagated into the steady state fluid concentrations to compare the concentration PDFs near the catalyst surface at the second and last teeth used in the gap-tooth method ( $z=125$  nm and  $z=L$ , respectively). Furthermore, as presented in Table 2, probabilistic bounds on the concentrations were computed at a 2% confidence level. The truncation errors of the PSE-based analyses compared to the multiscale model and the required computational times for each approach are also presented in this table. As shown in this table, the second-order PSE accurately describes the variability in the

**Table 2. Probabilistic Bounds and Computational Costs of the Steady State Fluid Concentrations Using MC Applied to the Primary Multiscale Model and the PSE-Based Approximations**

Method and species		$C_i^{lower}(z, L)$ (mM)		$C_i^{upper}(z, L)$ (mM)		Computational time (s)
		Second tooth ( $z = 125$ nm)	Last tooth ( $z = L$ )	Second tooth ( $z = 125$ nm)	Last tooth ( $z = L$ )	
MC applied to the primary multiscale model	A	240.58	238.58	240.85	240.06	6639
	B	240.58	238.60	240.84	240.06	
	C	0.1654	0.9693	0.4187	2.3977	
MC applied to the first-order PSE	A	240.56 (9.52%)	238.45 (9.19%)	240.81 (15.43%)	239.94 (8.28%)	182
	B	240.56 (10.15%)	238.46 (9.48%)	240.81 (13.28%)	239.90 (11.43%)	
	C	0.1816 (6.42%)	1.0619 (6.49%)	0.4243 (2.21%)	2.5479 (10.52%)	
MC applied to the second-order PSE	A	240.59 (2.37%)	238.63 (2.82%)	240.84 (4.15%)	240.10 (3.03%)	170
	B	240.58 (2.52%)	238.62 (1.56%)	240.84 (1.69%)	240.10 (2.43%)	
	C	0.1566 (3.45%)	0.9566 (0.88%)	0.4117 (2.75%)	2.3924 (0.37%)	



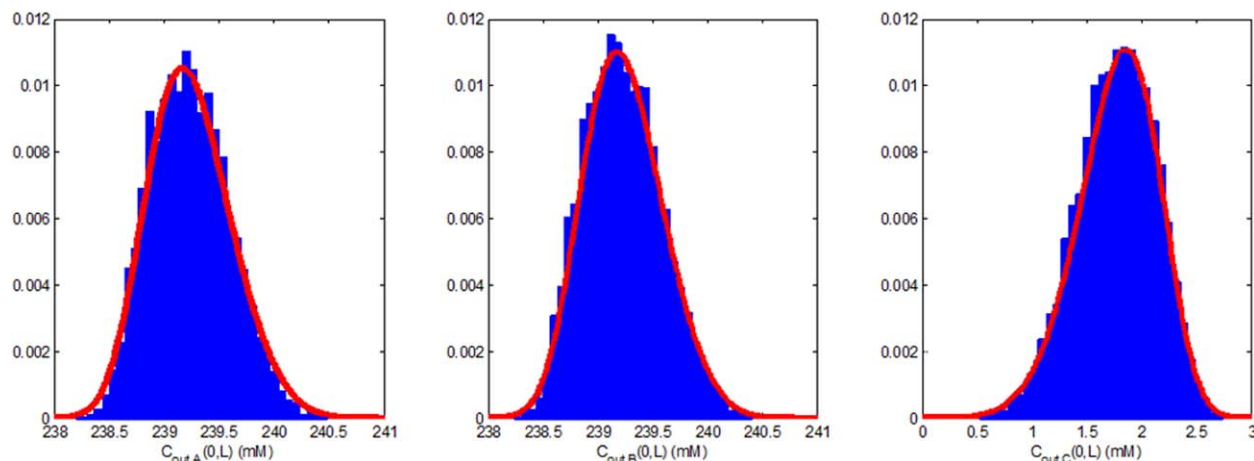


**Figure 7. PDFs of the steady state output concentrations  $C_{out,i}(0,L)$  generated by the primary multiscale model (blue) and second-order PSE (red).**

[Color figure can be viewed in the online issue, which is available at [wileyonlinelibrary.com](http://wileyonlinelibrary.com).]

reactor's fluid concentrations, as the errors in the second-order PSE are relatively small (less than  $\pm 5\%$ ). Furthermore, Figure 6 demonstrates that, while the first-order PSE is unable to describe the shape of the PDF tails, second-order PSE can accurately capture the tails of the output distribution. As a result, truncation errors of the first-order PSE relative to the primary model are notably larger, averaging around  $\pm 9\%$  (see Table 2). Both PSE-based approaches are substantially less time-consuming compared to the primary multiscale model, with little difference between the times for the first and second-order PSEs. Accordingly, the second-order PSE-based approach was implemented in this work to study the effects of uncertainty on the catalytic reactor. It is important to note that the method presented in this work for uncertainty propagation can be employed regardless of the type of the probabilistic description imposed on the uncertain parameters.

## Results and Discussion

### Uncertainty analysis

The PSE-based algorithm described above was used to propagate key parameter uncertainties in the porous catalytic reactor model described in the "Model Development" section. The following three scenarios were considered in this work: an uncertainty analysis of a reactor with a known catalyst pore size and three uncertain kinetic parameters, an uncertainty analysis of a reactor where the catalyst pore size was not known with certainty in addition to three uncertain kinetic parameters, and an extension of the uncertainty analysis to encompass all uncertain model parameters. In all three scenarios, the effects of uncertainty were considered in the species concentrations at eight axial points with coordinates ( $y=R, z=z_{ij}$ ), where  $z_{ij}$  corresponds to the location of each tooth used in the gap-tooth method. The effects of uncertainty were also analyzed in the reactor output concentrations,  $C_{out,i}(0,L)$ . The variation in the effects of uncertainty on the fluid concentrations were considered at four equidistant radial points with coordinates ( $y=y_{ii}, z=L$ ), where  $y_{ii} = \{0 \text{ nm}, 3.33 \text{ nm}, 6.67 \text{ nm}, 10 \text{ nm}\}$ . Probabilistic bounds for each scenario were calculated at a confidence level of 2%. The results obtained from these scenarios are discussed in the next sections.

### Scenario 1: uncertainty analysis on the catalytic reactor with known pore size

Uncertainty in key system parameters was propagated to the fluid concentrations inside the catalytic reactor. The key parameters were identified prior to the analysis by performing an offline sensitivity analysis on each model parameter. The sensitivity analysis was conducted by varying each of the multiscale model parameters independently by  $\pm 25\%$  and  $\pm 50\%$ . The results from this analysis were used to determine how sensitive the output concentrations are to each of the uncertain parameters. Note that the temperature, the inlet fluid velocity, the length, and the radius of the pores in the catalytic reactor, i.e., the operating conditions and design parameters, remained constant during this analysis and were set to the nominal values reported in Table 1. From this analysis, it was determined that the activation energies of desorption for species A and reaction, i.e.,  $E_{d,A}$  and  $E_r$ , have the largest overall effect on the system. Uncertainty was also applied to the adsorption constant  $k_{d,A}$  as it is the key parameter affecting the adsorption rate of species A. Parameter uncertainty descriptions can be obtained from experiments or DFT simulations.<sup>69–72</sup> A multivariate normal PDF is often regarded as a practical approximation to describe the parametric uncertainty in most engineering applications. Accordingly, the key uncertain parameters considered in this work were assumed to be normally distributed around the mean values of  $[\hat{k}_{d,A}, \hat{E}_{d,A}, \hat{E}_r] = [1, 95, 57]$  with the following covariance matrix:

$$\mathbf{V}(k_{d,A}, E_{d,A}, E_r) = \begin{bmatrix} 0.01 & 0.005 & 0.005 \\ 0.005 & 8.1225 & 1.46205 \\ 0.005 & 1.46205 & 2.9241 \end{bmatrix} \quad (20)$$

Figure 7 displays the effects of the uncertainty on the output fluid concentrations  $C_{out,i}(0,L)$  for each chemical species, determined using both the primary multiscale reactor model and the second-order PSE. The probabilistic bounds are presented in Table 3 alongside the computational times required by each method. As shown, uncertainty in these kinetic model parameters results in substantial variability in the concentrations. This is especially apparent in product C, where the probabilistic bounds show that the concentration can deviate from

**Table 3. Distributional Uncertainty Analysis, Scenario 1**

Method	Species	$C_{out,i}^{lower}(0, L)$ (mM)	$C_{out,i}^{upper}(0, L)$ (mM)	Nominal concentration (mM)	Computational time (s)
MC applied to the Primary Multiscale Model	A	238.51	240.17	239.18	10812
	B	238.52	240.11	239.22	
	C	0.8990	2.4961	1.8022	
MC applied to the Second-Order PSE	A	238.42 (4.87%)	240.16 (1.15%)	239.18	1193
	B	238.45 (4.22%)	240.09 (0.83%)	239.22	
	C	0.9116 (0.79%)	2.5689 (4.56%)	1.8022	

45 to 65% of its predicted mean value, as shown in Table 3. Furthermore, the second-order PSE approximation can accurately describe the uncertainty propagation through the porous catalytic reactor model using only 11% of the computational cost required by the MC sampling method when applied to the primary multiscale model.

Figure 8a shows the concentration PDFs for each chemical species along the radial direction at the reactor outlet  $C_i(y_{ti}, L)$ , which were determined using second-order PSE. This figure reveals that the concentrations do not significantly change along the reactor's radial domain. As a result, for brevity, the uncertainty propagation in the radial direction is not considered in the remainder of this work. Additionally, Figure 8b shows the concentration PDFs of each chemical species at the catalyst surface along the reactor's axial direction, i.e.,  $C_i(R, z_{ij})$ . As shown in this figure, the uncertainties are propagated in the axial direction, resulting in more variability in the steady state concentrations toward the end of the pore. The propagation of uncertainty implies that the variability in the output concentrations can be reduced by shortening the lengths of the reactor pores. This is at the expense of reducing the production of species C, and results in decreased reactor productivity.

### Scenario 2: uncertainty analysis on the catalytic reactor with uncertain pore size

The results discussed in the previous subsection assumed that the pore size is known with certainty. Experimental observations have demonstrated that the shape and size of a nanopore can deviate significantly from their expected value,<sup>73</sup> as the dimensions of a nanopore cannot be precisely determined through experimental observations. Furthermore, the size of the nanopores in the catalytic reactor has a substantial effect on the reactor performance as demonstrated at the end of the "Model Development" section. Therefore, uncertainty in the pore size should be taken into account when assessing the performance of this type of catalytic systems. Taking this into consideration, uncertainty analysis was also performed on a catalytic reactor where the pore size is assumed to be uncertain. For this analysis, both the pore radius and the set of kinetic parameters studied in Scenario 1 were considered as the set of uncertain parameters. The pore radius was assumed to be normally distributed with a mean value of  $\hat{r} = 10$  nm and a standard deviation of 20% of the mean value. This assumption was based on a previous study performed on the pore size

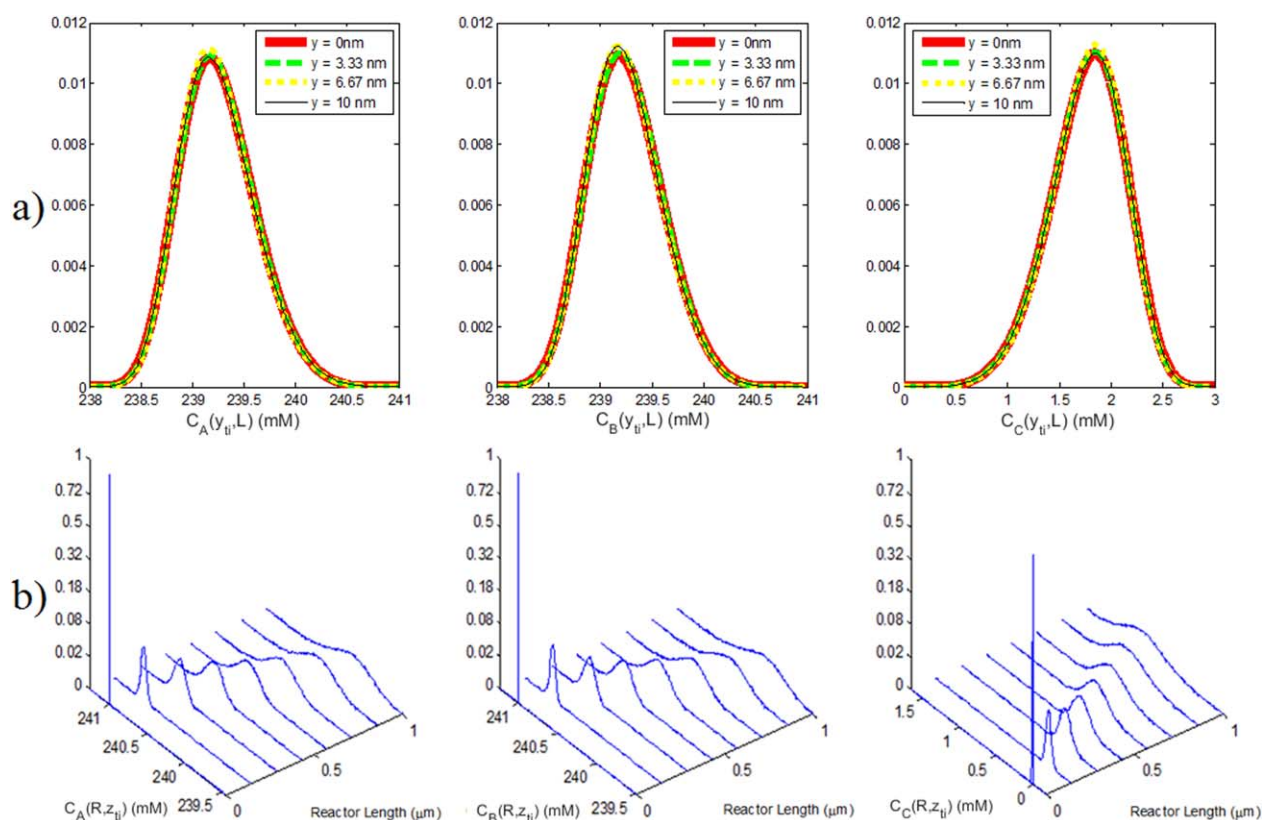


**Figure 8. PDFs of the concentration for each chemical species (a) along the radial direction at the reactor outlet ( $C_i(y_{ti}, L)$ ), and (b) along the axial direction within the reactor interior ( $C_i(R, z_{ti})$ ).**

[Color figure can be viewed in the online issue, which is available at [wileyonlinelibrary.com](http://wileyonlinelibrary.com).]

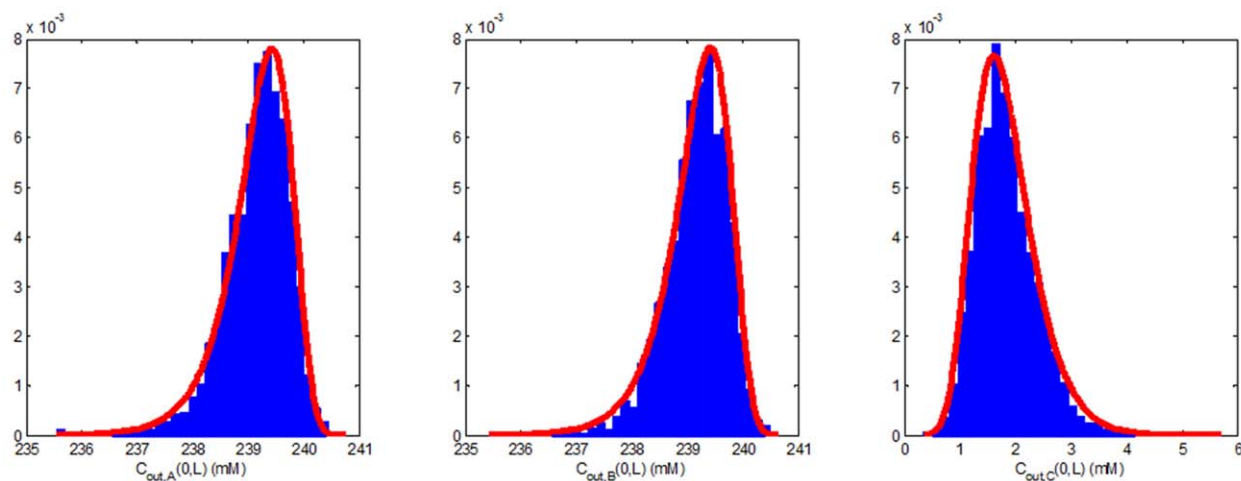


**Figure 9.** PDFs of the output fluid concentrations  $C_{out,i}(0,L)$  using MC applied to the primary multiscale model (blue) and the second-order PSE (red).

[Color figure can be viewed in the online issue, which is available at [wileyonlinelibrary.com](http://wileyonlinelibrary.com).]

distribution of nanoporous alumina.<sup>73</sup> The key kinetic parameters were assumed to follow the same normal distribution as described in the previous subsection. Figure 9 shows the effect of parameter uncertainties on the output species concentrations  $C_{out,i}(0,L)$  determined using the primary multiscale reactor model and the second-order PSE. A comparison of the mean values, probabilistic bounds, nominal model parameter values, and computational times is also presented in Table 4. The results show that the second-order PSE is capable of capturing the effect of uncertainties in the pore radius in addition to the key kinetic parameters. The errors in the bounds obtained from the second-order PSE are within  $\pm 5\%$ , and the PSE-based uncertainty analysis requires 16% of the computational time required using MC applied to the primary multiscale model. Figure 10a compares the PDFs of the output concentration  $C_{out,i}(0,L)$  for the cases of known and uncertain pore radius sizes. This figure reveals that uncertainty in the pore radius has a significant effect on the shape and bounds of the steady state concentration profiles thus affecting the reactor performance. In particular, when the probabilistic bounds listed in Tables 3 and 4 are compared, the lower bounds for species A and B decrease by  $984 \mu\text{M}$  while the upper bounds for species C increased by  $892 \mu\text{M}$  when the pore radius is assumed to be uncertain. Figure 10b, conversely, shows the PDFs of the axial concentrations along the reactor length  $C_i(R, z_{ij})$  for reactors with known and uncertain pore radius size. This figure demonstrates notably wider PDFs throughout the reactor for each chemical species for the case when the pore radius is uncertain.

### Scenario 3: uncertainty analysis on the catalytic reactor for all uncertain parameters

The previous scenarios presented in this work have only considered uncertainty in the pore radius and three kinetic parameters. The aim of this scenario is to evaluate the effects of considering additional uncertain parameters into the analysis. Accordingly, two analyses were performed using six and ten uncertain parameters, respectively. For the six parameter case study, uncertainty was considered in the pore radius in addition to the five kinetic parameters which had the largest effect on the concentrations, i.e.,  $k_{a,A}$ ,  $k_{a,B}$ ,  $E_{d,A}$ ,  $E_{d,B}$ , and  $E_r$ . The uncertain kinetic parameters were assumed to be normally distributed around their mean values as listed in Table 1, with the following covariance matrix:

$$\mathbf{V}(k_{a,A}, k_{a,B}, E_{d,A}, E_{d,B}, E_r, r) = \begin{bmatrix} 0.01 & 0.005 & 0.005 & 0.005 & 0.005 & 0 \\ 0.005 & 0.01 & 0.005 & 0.005 & 0.005 & 0 \\ 0.005 & 0.005 & 8.1225 & 4.06125 & 1.46205 & 0 \\ 0.005 & 0.005 & 4.06125 & 9 & 1.46205 & 0 \\ 0.005 & 0.005 & 1.46205 & 1.46205 & 2.9241 & 0 \\ 0 & 0 & 0 & 0 & 0 & 4 \times 10^{-18} \end{bmatrix} \quad (21)$$

**Table 4.** Distributional Uncertainty Analysis, Scenario 2

Method	Species	$\hat{C}_{out,i}(0,L)$ (mM)	$C_{out,i}^{lower}(0,L)$ (mM)	$C_{out,i}^{upper}(0,L)$ (mM)	Nominal concentration (mM)	Computational time (s)
MC applied to the primary multiscale model	A	239.16	237.38	240.19	239.18	10,898
	B	239.16	237.43	240.18	239.22	
	C	1.8461	0.8267	3.6036	1.8022	
MC applied to the second-order PSE	A	239.17 (0.36%)	237.40 (0.53%)	240.18 (0.41%)	239.18	1784
	B	239.16 (0.36%)	237.37 (2.30%)	240.16 (0.89%)	239.22	
	C	1.8377 (0.30%)	0.8185 (0.29%)	3.6013 (0.09%)	1.8022	



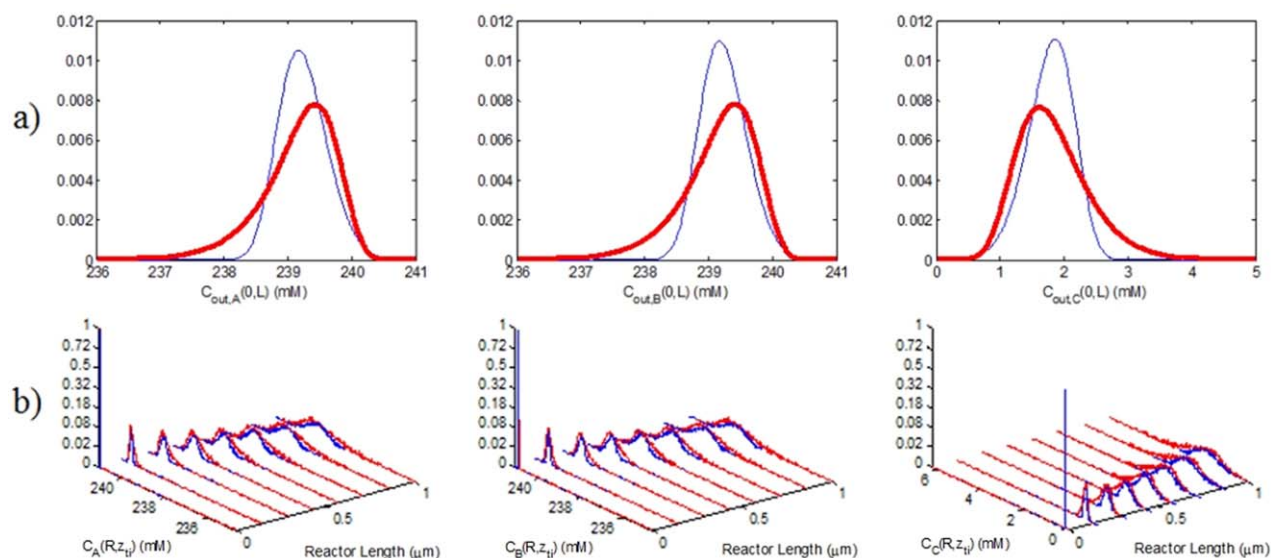


**Figure 10. PDFs of the (a) output fluid concentrations  $C_{out,i}(0,L)$  and (b) steady state fluid concentrations,  $C_i(R,z_{ij})$ , along the reactor axial length; pore radius fixed (blue) and uncertain (red).**

[Color figure can be viewed in the online issue, which is available at [wileyonlinelibrary.com](http://wileyonlinelibrary.com).]

The 10 uncertain parameter case study considered parametric uncertainty in all eight kinetic parameters in addition to uncertainty in the pore radius and the fluid diffusivity, i.e.,  $k_{a,A}$ ,  $k_{a,B}$ ,

$k_{d,A}$ ,  $k_{d,B}$ ,  $E_{d,A}$ ,  $E_{d,B}$ ,  $k_r$ ,  $E_r$ ,  $r$ , and  $D_i$ . All uncertain parameters were assumed to be normally distributed around their nominal values as listed in Table 1, with the following covariance matrix:

$$\mathbf{V}(k_{a,A}, k_{a,B}, k_{d,A}, k_{d,B}, E_{d,A}, E_{d,B}, k_k, E_r, r, D_i) = \begin{bmatrix} 0.01 & 0.005 & 0.005 & 0.005 & 0.005 & 0.005 & 0.005 & 0.005 & 0 & 0 \\ 0.005 & 0.01 & 0.005 & 0.005 & 0.005 & 0.005 & 0.005 & 0.005 & 0 & 0 \\ 0.005 & 0.005 & 1 \times 10^{20} & 5 \times 10^{19} & 4.06125 & 4.5 & 2 \times 10^{12} & 1.46205 & 0 & 0 \\ 0.005 & 0.005 & 5 \times 10^{19} & 1 \times 10^{20} & 4.06125 & 4.5 & 2 \times 10^{12} & 1.46205 & 0 & 0 \\ 0.005 & 0.005 & 4.06125 & 4.06125 & 8.1225 & 4.06125 & 4.06125 & 1.46205 & 0 & 0 \\ 0.005 & 0.005 & 4.5 & 4.5 & 4.06125 & 9 & 4.5 & 1.46205 & 0 & 0 \\ 0.005 & 0.005 & 2 \times 10^{12} & 2 \times 10^{12} & 4.06125 & 4.5 & 4 \times 10^{12} & 1.46205 & 0 & 0 \\ 0.005 & 0.005 & 1.46205 & 1.46205 & 1.46205 & 1.46205 & 1.46205 & 2.9241 & 0 & 0 \\ 0 & 0 & 0 & 0 & 0 & 0 & 0 & 0 & 4 \times 10^{-18} & 0 \\ 0 & 0 & 0 & 0 & 0 & 0 & 0 & 0 & 0 & 1.1236 \times 10^{-18} \end{bmatrix} \quad (22)$$

Figure 11 shows the effect of parametric uncertainties on the output concentration of species C,  $C_{out,C}(0,L)$  for both the six parameter and ten parameter uncertainty analyses, using MC applied to the primary multiscale model and second-order PSE approximations. The computational costs, mean, variance, and upper and lower bounds evaluated at a 2% confidence interval are presented in Table 5. Second-order PSE was chosen based on preliminary simulations using different PSE orders, which revealed that second-order PSE provides suitable results at acceptable computational costs. A total of 10,000 and 16,000 MC sampling points were applied to the primary multiscale model to capture the effects of uncertainties for six and ten uncertain parameters, respectively. The number of MC simulations was determined by adding sample

points to the analysis until the difference in the mean and variance of the PDFs in the outputs remained fairly constant, i.e., below 1% error between subsequent simulation runs.

The results from Figure 11 and Table 5 indicate that the second-order PSE is able to capture the output variability, as the PSE model errors for the mean and variance are below  $\pm 1\%$  while probabilistic bounds all remain within  $\pm 5\%$  of the bounds obtained from MC approach. MC sampling directly applied to the primary model required a CPU time that is 12 and 35 times larger than that needed by the second-order PSE functions, respectively. Accuracy may be slightly improved using higher order PSEs; however, it requires substantially larger computational cost due to the additional multiscale simulations necessary to calculate the higher order sensitivities.

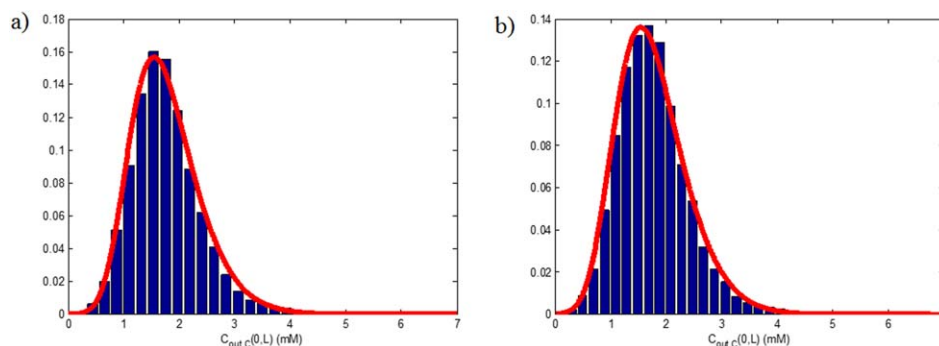


**Figure 11.** PDFs of the output fluid concentration for species C,  $C_{out,C}(0, L)$ , using MC applied to the primary multiscale model (blue) and the second-order PSE (red) for (a) six uncertain parameters and (b) ten uncertain parameters.

[Color figure can be viewed in the online issue, which is available at [wileyonlinelibrary.com](http://wileyonlinelibrary.com).]

Figure 11 illustrates that the addition of uncertain parameters produces slight changes in the shape of the concentration distributions. As shown in Tables 4 and 5, the lower and upper bounds deviated 230 and 57  $\mu\text{M}$ , respectively, between the output variability for the six and the four uncertain parameter cases; likewise, the lower and upper bounds deviated 18 and 47  $\mu\text{M}$ , respectively, between the six uncertain parameter case and the ten uncertain parameter case. Tables 4 and 5 also show that higher CPU times are required to compute the PSE-based model when additional uncertain parameters are included in the analysis as there are more input-output sensitivities that need to be estimated, thus requiring the need to perform additional sampling using the primary multiscale model. Figure 12 illustrates the effects of uncertainty on the concentration of species C as it varies along the axial reactor length,  $C_i(R, z_{ij})$ , when six and ten uncertain parameters are considered in the analysis. This figure reveals that the uncertainties are propagated axially, similar to the previous scenarios, resulting in larger variability at the pore outlet.

In the present scenario, the uncertainty in the pre-exponential factors for the desorption and reaction terms i.e.,  $k_{d,A}$ ,  $k_{d,B}$ , and  $k_r$ , were assumed to vary with a standard deviation of 10% of their nominal values. In principle, these terms can vary orders in magnitude from their corresponding expected values,<sup>53</sup> which could have a significant effect on the resulting output concentration profiles. To illustrate these effects, the standard deviations for the pre-exponential factors were increased from 10% to 32% of the corresponding nominal values, thus allowing these parameters to change by at least an order of magnitude with respect to their expected values. Figure 13 compares the concentration PDFs generated employing PSE approximation when the standard deviations of the pre-exponential factors are set to 10% and 32% of the nominal values, respectively, within the 10 uncertain parameter case study. Moreover, the difference in the mean, variance, and probabilistic bounds are listed in Table 6. These results indicate that larger variations in the pre-exponential factor have significant effects on the output concentrations, resulting in a 13% wider standard deviation and a 6.5% shift in the upper and lower bounds for the outlet concentration of species C.

### Robust optimization

Process optimization is often sought as a practical tool for performance improvement. The quality of the solution obtained from optimization is directly determined by the accuracy of the model being used to represent the system under analysis and the model parameters. The high-order models such as mechanistic models of large-scale or complex systems often cannot be embedded within an optimization framework due to prohibitive computational costs. In addition, model parameters are always subject to uncertainty thus adding complexity into the analysis. Instead, low-order models that capture the key system characteristics under parameter uncertainty are used in model-based optimization to improve the performance of the process.

To illustrate the benefits of the algorithm presented in this work for uncertainty quantification, the PSE-based framework was used to identify the optimal operating conditions on the multiscale catalytic flow reactor system that maximize productivity under uncertainty. As shown in the previous sections, the present heterogeneous multiscale reactor model is subject to product concentration variability due to uncertain realizations in the model parameters. Conversely, key operating conditions and design parameters such as the reactor's temperature ( $T$ ), inlet fluid velocity ( $u$ ), and the pore length ( $L$ ) can be adjusted to improve process productivity. Accordingly, a robust optimization formulation can be specified for this process and is as follows:

$$\begin{aligned} & \max_{T,L,u} w \hat{C}_{out,C}(0, L) - (1-w) \sigma_{out,C}^2(0, L) \\ & \text{Subject to:} \\ & \text{Multiscale model Eqs. 1–15} \\ & T_{\min} \leq T \leq T_{\max} \\ & L_{\min} \leq L \leq L_{\max} \\ & u_{\min} \leq u \leq u_{\max} \end{aligned} \quad (23)$$

where  $\hat{C}_{out,C}(0, L)$  represents the expected concentration of species C at the center of the pore outlet while  $\sigma_{out,C}^2(0, L)$  represents its variance. The parameter  $w$  is a weight that

**Table 5.** Distributional Uncertainty Analysis, Scenario 3

Method	Number of uncertain parameters	$\hat{C}_{out,C}(0, L)$ (mM)	$\sigma_{out,C}^2(0, L)$ (mM <sup>2</sup> )	$C_{out,C}^{lower}(0, L)$ (mM)	$C_{out,C}^{upper}(0, L)$ (mM)	Computational time (s)
MC applied to the primary multiscale model	6	1.7641	0.3907	0.5972	3.6995	68,623
	10	1.7673	0.3965	0.5817	3.7031	101,672
MC applied to the second-order PSE	6	1.7705 (0.21%)	0.3865 (1.06%)	0.5861 (0.36%)	3.5448 (4.98%)	2156
	10	1.7510 (0.47%)	0.3938 (0.38%)	0.5067 (3.51%)	3.5667 (4.55%)	5819

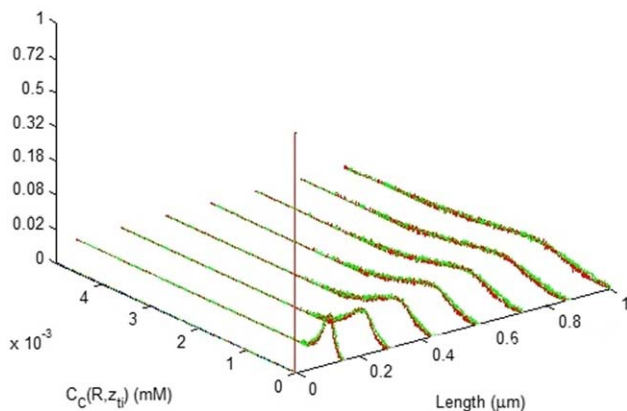


**Figure 12.** PDFs of the steady state fluid concentration for species C,  $C_C(R, z_{ti})$ , along the reactor axial length; six uncertain parameters (red) and ten uncertain parameters (green).

[Color figure can be viewed in the online issue, which is available at [wileyonlinelibrary.com](http://wileyonlinelibrary.com).]

determines the significance of the expected value and variance in the optimization formulation. In principle,  $\hat{C}_{out,C}(0, L)$  and  $\sigma_{out,C}^2(0, L)$  can be estimated through a large number of MC sampling points applied on the primary multiscale model. As shown in the results presented in the previous section, this approach is computationally prohibitive. Accordingly,  $\hat{C}_{out,C}(0, L)$  and  $\sigma_{out,C}^2(0, L)$  in (23) are calculated using a second-order PSE. That is, for each set of values in the optimization variables, a second-order PSE is built (using the primary multiscale model) to estimate  $\hat{C}_{out,C}(0, L)$  and  $\sigma_{out,C}^2(0, L)$ . Note that the primary multiscale model is only used in (23) to compute the sensitivities needed for the PSE approximations. In the present analysis, the weight  $w$  in (23) was set to 0.5. Furthermore, the three kinetic parameters  $k_{a,A}$ ,  $E_{d,A}$ ,  $E_r$ , and the pore radius  $r$  were considered as the uncertain parameters and were assumed to follow a normal distribution with the means and standard deviations defined as in *Scenario 2*. To compare the results obtained from (23), a similar problem was formulated under the assumption of perfect knowledge of the model parameters, i.e.,

$$\begin{aligned} & \max_{T, L, u} \hat{C}_{out,C}(0, L) \\ & \text{Subject to:} \\ & \text{Multiscale model Eqs. 1–15} \\ & T_{\min} \leq T \leq T_{\max} \\ & L_{\min} \leq L \leq L_{\max} \\ & u_{\min} \leq u \leq u_{\max} \end{aligned} \quad (24)$$

As shown in (24), only the expected value of the outlet concentration of species C is considered in the cost function. At each optimization step, simulations of the primary multiscale model were performed to compute  $\hat{C}_{out,C}(0, L)$ . For the two optimization problems shown in (23) and (24),  $T_{\min}$  and  $T_{\max}$  were set to 300 and 700 K while  $L_{\min}$  and  $L_{\max}$  were set to 0.5 and 1.5  $\mu\text{m}$  and  $u_{\min}$  and  $u_{\max}$  were set to 0.005 and 0.015 m/s, respectively.

The optimal reactor temperature, pore length, and fluid velocity obtained from the robust optimization formulation (MaxConc) and the nominal optimization formulation (Nomi-

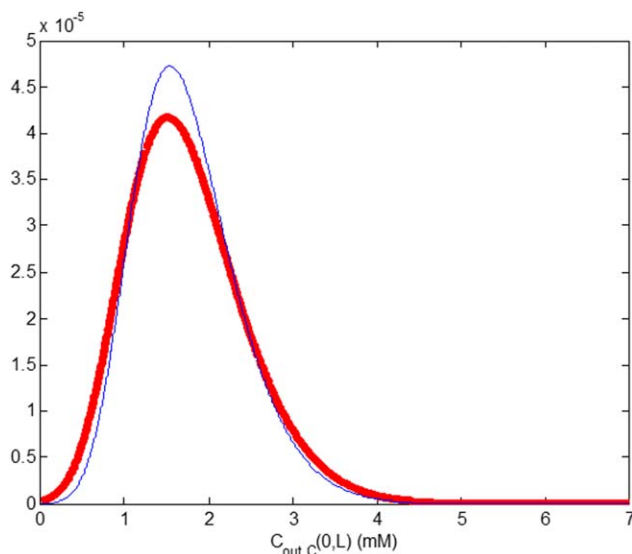


**Figure 13.** PDFs of the output fluid concentration for species C,  $C_{out,C}(0, L)$ , for ten uncertain parameters using standard deviations of 10% of the nominal values (blue) and 32% of the nominal values (red) in the pre-exponential factors.

[Color figure can be viewed in the online issue, which is available at [wileyonlinelibrary.com](http://wileyonlinelibrary.com).]

nal), i.e., problems (23) and (24) respectively, are shown in Table 7. The mean, variance, and probabilistic bounds at a 2% confidence interval for the species C concentration PDFs obtained using these two optimization formulations are also shown in Table 7. For the case of the nominal optimization, the statistics on the process outputs were obtained by performing MC sampling on the primary multiscale model using the uncertainty parameter descriptions used in the robust optimization formulation. As shown in Table 7, large pore lengths ( $L=L_{\max}$ ) and small fluid velocities ( $u=u_{\min}$ ) are needed to maximize the production of species C. Additionally, reasonably high temperatures maximize the number of reactions taking place on the surface to improve the production of species C. As shown in Figure 14, the concentration of species C experiences a maximum at  $T=466$  K, as predicted by the nominal optimization results. This optimal temperature is a result of the surface reaction ensembles necessary in order for reaction to occur. Initially, increasing the temperature will increase the rate of reaction, resulting in higher product concentrations; however, at sufficiently high temperatures, the increasing desorption rate significantly affects the number of surface reaction ensembles, which decreases the reaction rate.

**Table 6.** Distributional Pre-exponential Factor Uncertainty Analysis

Pre-exponential factor, standard deviation	$\hat{C}_{out,C}(0, L)$ (mM)	$\sigma_{out,C}^2(0, L)$ (mM <sup>2</sup> )	$C_{out,C}^{lower}(0, L)$ (mM)	$C_{out,C}^{upper}(0, L)$ (mM)
10% of the nominal values	1.7510	0.3938	0.5067	3.5667
32% of the nominal values	1.7425	0.5056	0.3045	3.7732



**Table 7. Nominal and Robust Optimization Results**

Optimization scenarios	$T$ (K)	$L$ ( $\mu\text{m}$ )	$u$ (mm/s)	$\hat{C}_{out,C}(0, L)$ (mM)	$\sigma_{out,C}^2(0, L)$ ( $\text{mM}^2$ )	$C_{out,C}^{lower}(0, L)$ (mM)	$C_{out,C}^{upper}(0, L)$ (mM)
Nominal optimization (nominal)	466	1.50	5.00	5.7568	3.4694	2.2658	11.2122
Robust optimization (MaxConc)	455	1.50	5.00	5.1949	3.3331	1.5345	10.3859
Robust optimization (MinVar)	466	1.44	5.54	5.0185	2.6944	2.0069	9.9064

The results for the robust optimization under uncertainty (MaxConc in Table 7) indicate that a lower reactor temperature, with the same pore length and inlet velocity as that obtained from the nominal optimization, is needed to account for parameter uncertainty. As shown in Table 7, accounting for the variance in the outlet concentration due to parameter uncertainty results in a 9.76% and 3.92% decrease in the mean and variance of the product concentration, respectively, when compared to the nominal optimization. Figure 15 depicts the outlet concentration PDFs of species C from both the robust optimization formulation (MaxConc) and the nominal optimization formulation (Nominal). This figure shows that product variability can be reduced at the expense of reducing production of species C. To further investigate this condition, an additional robust optimization problem was formulated to minimize product variability under specific production constraints in the presence of uncertainty, i.e.,

$$\begin{aligned}
 & \min_{T, L, u} \sigma_{out,C}^2(0, L) \\
 & \text{Subject to:} \\
 & \text{Multiscale model Eqs. 1–15} \\
 & \hat{C}_{out,C}(0, L) \geq \hat{C}_{out,C}^*(0, L) \\
 & T_{\min} \leq T \leq T_{\max} \\
 & L_{\min} \leq L \leq L_{\max} \\
 & u_{\min} \leq u \leq u_{\max}
 \end{aligned} \quad (25)$$

where  $\hat{C}_{out,C}^*(0, L)$  represents a minimum acceptable concentration of species C on average, which was set to 5 mM for this problem. Similar to the robust optimization problem (23), a second-order PSE was used to evaluate  $\hat{C}_{out,C}(0, L)$  and  $\sigma_{out,C}^2(0, L)$ . Additionally, the same uncertain parameter

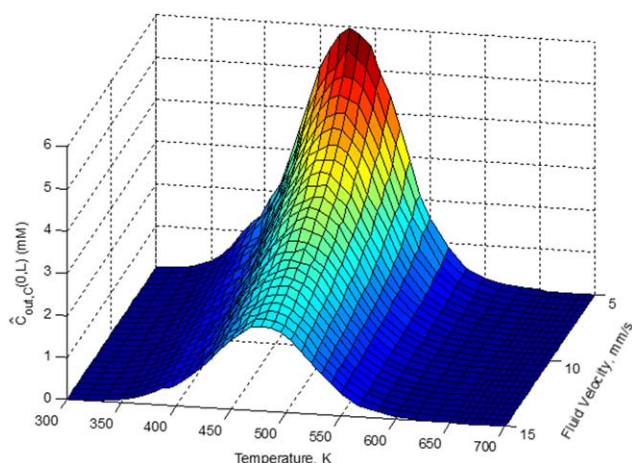


**Figure 14. Nominal outlet fluid concentration for species C,  $\hat{C}_{out,C}(0, L)$ , as a function of temperature  $T$  and fluid velocity  $u$ ; pore length,  $L = 1.5 \mu\text{m}$ .**

[Color figure can be viewed in the online issue, which is available at [wileyonlinelibrary.com](http://wileyonlinelibrary.com).]

descriptions used to solve problem (23) were applied in this problem. The results from this optimization formulation are presented in Table 7 (MinVar) and Figure 15. These results reveal a 22.3% decrease in the variance of the concentration PDF for species C when compared to the nominal optimization results; accordingly, the upper and lower bounds computed from the results of this robust optimization problem (MinVar) are 10.4% and 13.7% closer to its mean value when compared to the bounds obtained from the nominal optimization formulation (Nominal). Note that the mean value in the production of species C obtained from MinVar is close to the production constraint considered in problem (25). These product specifications are obtained at approximately the same temperature as the nominal optimization results, but with a 60 nm shorter pore length and with a 0.54 mm/s faster inlet fluid velocity. Figure 15 clearly indicates that the results obtained from problem (25) produce a narrower distribution centered on its mean production value when compared to the distributions obtained from problems (23) and (24). These results show that parameter uncertainty play a key role and must be taken into account for process improvement in multiscale systems.

## Conclusions

This study presents an uncertainty analysis in the spatial domain of a heterogeneous multiscale catalytic reactor. To that extent, a porous catalytic flow reactor is modeled using a multiscale approach where the continuum conservation

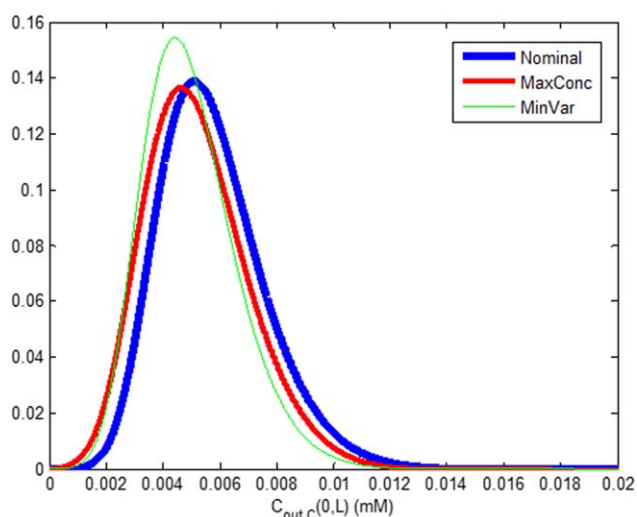


**Figure 15. PDFs of the output fluid concentration for species C,  $\hat{C}_{out,C}(0, L)$ , at the nominal optimization conditions (Nominal, blue) and the robust optimization formulations, i.e., MaxConc (red) and MinVar (green).**

[Color figure can be viewed in the online issue, which is available at [wileyonlinelibrary.com](http://wileyonlinelibrary.com).]

equations that describe the fluid phase behavior are coupled with a lattice-based KMC model to capture the phenomena on the catalyst surface. A PSE-based framework is employed to propagate uncertainties throughout the spatial domain of the reactor model. Moreover, an uncertainty analysis is performed on a reactor where the pore size is not known with certainty. These analyses show that parameter uncertainty has a substantial effect on the performance of spatially heterogeneous catalytic reactors, and cannot be neglected in their design. These effects remain significant even when 10 uncertain parameters are included, illustrating the necessity to account for all uncertain parameters. The potential of the techniques presented in this work was analyzed through the application to a robust optimization formulation. The results obtained for the present heterogeneous multiscale catalytic reactor flow system show that taking uncertainty into account can specify suitable operating conditions that reduce product variability at the expense of lower production. While the present analysis utilized PSE as the uncertainty quantification method, other methods such as non-intrusive PCE can also be employed to analyze uncertainty propagation in multiscale systems. A comparison that explores the benefits and limitations of each method in systems that are not available in closed-form models, such as the present heterogeneous multiscale system, is considered as part of the future work in this research.

## Acknowledgment

The financial support provided by the Natural Sciences and Engineering Research Council of Canada (NSERC) is gratefully acknowledged.

## Literature Cited

- Bournay L, Casanave D, Delfort B, Hillion G, Chodorge JA. New heterogeneous process for biodiesel production: a way to improve the quality and the value of the crude glycerin produced by biodiesel plants. *Catal Today*. 2005;106(1–4):190–192.
- Chen B, Parker G, Han J, Meyyappan M, Cassell AM. Heterogeneous single-walled carbon nanotube catalyst discovery and optimization. *Chem Mater*. 2002;14(4):1891–1896.
- Senkan SM, Ozturk S. Discovery and optimization of heterogeneous catalysts by using combinatorial chemistry. *Angew Chem Int Ed*. 1999;38(6):791–795.
- Elnashaie SSEH, Elshishini SS. *Modelling, Simulation and Optimization of Industrial Fixed Bed Catalytic Reactors*. London: Gordon & Breach, 1993.
- Vlachos DG, Mhadeshwar AB, Kaisare NS. Hierarchical multiscale model-based design of experiments, catalysts, and reactors for fuel processing. *Comput Chem Eng*. 2006;30(10–12):1712–1724.
- Istadi I, Amin NAS. Modelling and optimization of catalytic-dielectric barrier discharge plasma reactor for methane and carbon dioxide conversion using hybrid artificial neural network—genetic algorithm technique. *Chem Eng Sci*. 2007;62(23):6568–6581.
- Jirát J, Kubíček M, Marek M. Mathematical modelling of catalytic monolithic reactors with storage of reaction components on the catalyst surface. *Catal Today*. 1999;53(4):583–596.
- Champagnie AM, Tsotsis TT, Minet RG, Wagner E. The study of ethane dehydrogenation in a catalytic membrane reactor. *J Catal*. 1992;134(2):713–730.
- Hayes RE, Kolaczowski ST, Thomas WJ. Finite-element model for a catalytic monolith reactor. *Comput Chem Eng*. 1992;16(7):645–657.
- Raimondeau S, Vlachos DG. Recent developments on multiscale, hierarchical modeling of chemical reactors. *Chem Eng J*. 2002;90(1–2):3–23.
- Ricardez-Sandoval LA. Current challenges in the design and control of multiscale systems. *Can J Chem Eng*. 2011;89(6):1324–1341.
- Christofides PD, Armaou A. Control and optimization of multiscale process systems. *Comput Chem Eng*. 2006;30(10–12):1670–1686.
- Christofides PD, Armaou A, Lou Y, Varshney A. *Control and Optimization of Multiscale Process Systems*. Boston, MA: Birkhäuser; 2008.
- Kwon JS-I, Nayhouse M, Orkoulas G, Ni D, Christofides PD. Run-to-run-based model predictive control of protein crystal shape in batch crystallization. *Ind Eng Chem Res*. 2015;54(16):4293–4302.
- Kwon JS-I, Nayhouse M, Christofides PD. Detection and isolation of batch-to-batch parametric drift in crystallization using in-batch and post-batch measurements. *Ind Eng Chem Res*. 2015;54(20):5514–5526.
- Drews TO, Webb EG, Ma DL, Alameda J, Braatz RD, Alkire RC. Coupled mesoscale—continuum simulations of copper electrodeposition in a trench. *AIChE J*. 2004;50(1):226–240.
- Rusli E, Drews TO, Ma DL, Alkire RC, Braatz RD. Nonlinear feedback control of a coupled kinetic Monte Carlo-finite difference code. *Proceed IFAC Symp ADCHEM*. 2003; 597–602.
- Vlachos DG. Multiscale integration hybrid algorithms for homogeneous–heterogeneous reactors. *AIChE J*. 1997;43(11):3031–3041.
- Matera S, Reuter K. Transport limitations and bistability for *in situ* CO oxidation at RuO<sub>2</sub> (110) : first-principles based multiscale modeling. *Phys Rev B*. 2010;82(8):085446.
- Mei D, Lin G. Effects of heat and mass transfer on the kinetics of CO oxidation over RuO<sub>2</sub>(110) catalyst. *Catal Today*. 2011;165(1):56–63.
- Kwon JS-I, Nayhouse M, Christofides PD. Multiscale, multidomain modeling and parallel computation: application to crystal shape evolution in crystallization. *Ind Eng Chem Res*. 2015;54(47):11903–11914.
- Vlachos DG. A review of multiscale analysis: examples from systems biology, materials engineering, and other fluid–surface interacting systems. *Adv Chem Eng*. 2005;30:1–61.
- Croze M, Sang-Il Kwon J, Nayhouse M, Ni D, Christofides PD. Multiscale modeling and operation of PECVD of thin film solar cells. *Chem Eng Sci*. 2015;136:50–61.
- Majumder D, Broadbelt LJ. A multiscale scheme for modeling catalytic flow reactors. *AIChE J*. 2006;52(12):4214–4228.
- Schaefer C, Jansen APJ. Coupling of kinetic Monte Carlo simulations of surface reactions to transport in a fluid for heterogeneous catalytic reactor modeling. *J Chem Phys*. 2013;138(5):054102.
- Siettos CI, Armaou A, Makeev AG, Kevrekidis IG. Microscopic/stochastic timesteppers and “coarse” control: a KMC example. *AIChE J*. 2003;49(7):1922–1926.
- Armaou A, Siettos C, Kevrekidis I. Time-steppers and “coarse” control of distributed microscopic processes. *Int J Robust Nonlinear Control*. 2004;14(2):89–111.
- Prasad V, Karim AM, Arya A, Vlachos DG. Assessment of overall rate expressions and multiscale, microkinetic model uniqueness via experimental data injection: ammonia decomposition on Ru/ $\gamma$ -Al<sub>2</sub>O<sub>3</sub> for hydrogen production. *Ind Eng Chem Res*. 2009;48(11):5255–5265.
- Li J, Croiset E, Ricardez-Sandoval L. Effect of carbon on the Ni catalyzed methane cracking reaction: a DFT study. *Appl Surf Sci*. 2014;311:435–442.
- Saliccioli M, Stamatakis M, Caratzoulas S, Vlachos DG. A review of multiscale modeling of metal-catalyzed reactions: mechanism development for complexity and emergent behavior. *Chem Eng Sci*. 2011;66(19):4319–4355.
- Allen JK, Seepersad C, Choi H, Mistree F. Robust design for multiscale and multidisciplinary applications. *J Mech Des*. 2006;128(4):832–843.
- Evans RD, Ricardez-Sandoval LA. Multi-scenario modelling of uncertainty in stochastic chemical systems. *J Comput Phys*. 2014;273:374–392.
- Patwardhan RS, Shah SL, Qi KZ. Assessing the performance of model predictive controllers. *Can J Chem Eng*. 2002;80(5):954–966.
- Selvanathan S, Tangirala AK. Diagnosis of poor control loop performance due to model–plant mismatch. *Ind Eng Chem Res*. 2010;49(9):4210–4229.
- Rasoulilian S, Ricardez-Sandoval LA. Uncertainty analysis and robust optimization of multiscale process systems with application to epitaxial thin film growth. *Chem Eng Sci*. 2014;116:590–600.
- Rasoulilian S, Ricardez-Sandoval LA. A robust nonlinear model predictive controller for a multiscale thin film deposition process. *Chem Eng Sci*. 2015;136:38–49.
- Kwon JS-I, Nayhouse M, Orkoulas G, Ni D, Christofides PD. A method for handling batch-to-batch parametric drift using moving horizon estimation: application to run-to-run MPC of batch crystallization. *Chem Eng Sci*. 2015;127:210–219.

38. Nagy ZK, Braatz RD. Distributional uncertainty analysis using power series and polynomial chaos expansions. *J Process Control*. 2007;17(3):229–240.
39. Nagy ZK, Braatz RD. Distributional uncertainty analysis of a batch crystallization process using power series and polynomial chaos expansions. *Proc 8th IFAC Symp ADCHEM*, 2006;655–660.
40. Hukkanen EJ, Braatz RD. Worst-case and distributional robustness analysis of the full molecular weight distribution during free radical bulk polymerization. *Proc ACC*, 2005;3115–3120.
41. Nagy ZK. Model based robust batch-to-batch control of particle size and shape in pharmaceutical crystallization. *9th Proc Int Fed Autom Cont. Symp Adv Contr Chem Process*, 2009;12–15.
42. Nagy ZK, Mahn B, Franke R, Allgöwer F. Nonlinear model predictive control of batch processes: an industrial case study. *16th IFAC World Congress*, 2005;4–8.
43. Nagy ZK, Braatz RD. Open-loop and closed-loop robust optimal control of batch processes using distributional and worst-case analysis. *J Process Control*. 2004;14(4):411–422.
44. Kumar D, Budman H. Robust nonlinear MPC based on Volterra series and polynomial chaos expansions. *J Process Control*. 2014;24(1):304–317.
45. Mandur J, Budman H. A polynomial-chaos based algorithm for robust optimization in the presence of bayesian uncertainty. *8th Ifac Symp ADCHEM*, 2012;549–554.
46. Mesbah A, Streif S, Findeisen R, Braatz R. Stochastic nonlinear model predictive control with probabilistic constraints. *Proc ACC*, 2014;2413–2419.
47. Drews TO, Braatz RD, Alkire RC. Parameter sensitivity analysis of Monte Carlo simulations of copper electrodeposition with multiple additives. *J Electrochem Soc*. 2003;150(11):C807–C812.
48. McGill JA, Ogunnaike BA, Vlachos DG. Efficient gradient estimation using finite differencing and likelihood ratios for kinetic Monte Carlo simulations. *J Comput Phys*. 2012;231(21):7170–7186.
49. Rasoulia S, Ricardez-Sandoval LA. Worst-case and distributional robustness analysis of a thin film deposition process. *9th Int Symp ADCHEM*, 2015;1127–1132.
50. Rasoulia S, Ricardez-Sandoval LA. Robust multivariable estimation and control in an epitaxial thin film growth process under uncertainty. *J Process Control*. 2015;34:70–81.
51. Rasoulia S, Ricardez-Sandoval L. Stochastic nonlinear model predictive control applied to a thin film deposition process under uncertainty. *Chem Eng Sci*. 2016;140:90–103.
52. Nagy ZK, Allgöwer F. A nonlinear model predictive control approach for robust end-point property control of a thin-film deposition process. *Int J Robust Nonlinear Control*. 2007;17(17):1600–1613.
53. Ulissi Z, Prasad V, Vlachos DG. Effect of multiscale model uncertainty on identification of optimal catalyst properties. *J Catal*. 2011;281(2):339–344.
54. Raimondeau S, Vlachos DG. The role of adsorbate-layer nonuniformities in catalytic reactor design: multiscale simulations for CO oxidation on Pt. *Comput Chem Eng*. 2002;26(7–8):965–980.
55. Dooling DJ, Broadbelt LJ. Generic Monte Carlo tool for kinetic modeling. *Ind Eng Chem Res*. 2001;40(2):522–529.
56. Makeev AG, Maroudas D, Panagiotopoulos AZ, Kevrekidis IG. Coarse bifurcation analysis of kinetic Monte Carlo simulations: a lattice-gas model with lateral interactions. *J Chem Phys*. 2002;117(18):8229.
57. Oveasson S, Lundqvist BI, Schneider WF, Bogicevic A. NO oxidation properties of Pt(111) revealed by *ab initio* kinetic simulations. *Phys Rev B*. 2005;71(11):115406.
58. Lam R, Vlachos DG. Multiscale model for epitaxial growth of films: growth mode transition. *Phys Rev B*. 2001;64(3):035401.
59. Gear CW, Li J, Kevrekidis IG. The gap-tooth method in particle simulations. *Phys Lett A*. 2003;316(3–4):190–195.
60. Kevrekidis IG, Gear CW, Hyman JM, et al. Equation-free, coarse-grained multiscale computation: enabling microscopic simulators to perform system-level analysis. *Commun Math Sci*. 2003;1(4):715–762.
61. Armaou A, Kevrekidis IG, Theodoropoulos C. Equation-free gap-tooth-based controller design for distributed complex/multiscale processes. *Comput Chem Eng*. 2005;29(4):731–740.
62. Samaey G, Roose D, Kevrekidis IG. The gap-tooth scheme for homogenization problems. *Multiscale Model Simul*. 2005;4(1):278–306.
63. Roberts AJ, Kevrekidis IG. Higher order accuracy in the gap-tooth scheme for large-scale dynamics using microscopic simulators. *ANZIAM J*. 2005;46:637–657.
64. Lou Y, Christofides PD. Feedback control of growth rate and surface roughness in thin film growth. *AIChE J*. 2003;49(8):2099–2113.
65. Mandreoli L, Neugebauer J, Kunert R, Schöll E. Atom density kinetic Monte Carlo: A hybrid approach to perform epitaxial growth simulations. *Phys Rev B*. 2003;68(15):155429.
66. Tsalikis D, Baig C, Mavrantzas VG, Amanatides E, Mataras D. Hierarchical simulation of microcrystalline PECVD silicon thin film growth and structure. *PSE2012*, 2012.
67. Bahakim SS, Rasoulia S, Ricardez-Sandoval LA. Optimal design of large-scale chemical processes under uncertainty: A ranking-based approach. *AIChE J*. 2014;60(9):3243–3257.
68. Paulson JA, Mesbah A, Streif S, Findeisen R, Braatz RD. Fast stochastic model predictive control of high-dimensional systems. *IEEE*; 2014:2802–2809.
69. Li J, Croiset E, Ricardez-Sandoval L. Carbon nanotube growth: first-principles-based kinetic Monte Carlo model. *J Catal*. 2015;326:15–25.
70. Reuter K, Scheffler M. First-principles kinetic Monte Carlo simulations for heterogeneous catalysis: Application to the CO oxidation at Ru O 2 (110). *Phys Rev B*. 2006;73(4):045433.
71. Hong S, Karim A, Rahman TS, Jacobi K, Ertl G. Selective oxidation of ammonia on RuO2(110): a combined DFT and KMC study. *J Catal*. 2010;276(2):371–381.
72. Fichthorn KA, Weinberg WH. Theoretical foundations of dynamical Monte Carlo simulations. *J Chem Phys*. 1991;95(2):1090–1096.
73. Kuang D, Charrière R, Matsapey N, Flury M, Faucheu J, Chavel P. Modeling the specular spectral reflectance of partially ordered alumina nanopores on an aluminum substrate. *Opt Express*. 2015;23(4):4506.

Manuscript received Nov. 18, 2015, and revision received Feb. 6, 2016.